JGR Solid Earth

RESEARCH ARTICLE
10.1029/2020JB019768

Stress Field Interactions Between Overlapping Shield Volcanoes: Borehole Breakout Evidence From the Island of Hawai'i, USA

Simona Pierdominici[1], John M. Millett[2,3], Jochem K. M. Kück[1], Donald Thomas[4], Dougal A. Jerram[5,6], Sverre Planke[2,5], Eric Haskins[7], Nicole Lautze[4], and Olivier Galland[8]

[1]Helmholtz Centre Potsdam GFZ German Research Centre for Geosciences, Potsdam, Germany, [2]Volcanic Basin Petroleum Research (VBPR), Oslo, Norway, [3]Department of Geology and Geophysics, University of Aberdeen, Aberdeen, UK, [4]Hawai'i Institute of Geophysics and Planetology, University of Hawai'i at Manoa, Honolulu, HI, USA, [5]Centre for Earth Evolution and Dynamics (CEED), University of Oslo, Oslo, Norway, [6]DougalEARTH Ltd., Solihull, UK, [7]University of Hawai'i at Hilo, Center for Study of Active Volcanoes (CSAV), Hilo, HI, USA, [8]NJORD Center, Department of Geosciences, University of Oslo, Oslo, Norway

Key Points:
- First documentation of the subsurface in situ stress state between the major island forming shield volcanoes of Mauna Loa and Mauna Kea
- Borehole breakouts analysis constrains the present-day stress field between large shield volcanoes on the island of Hawai'i
- Stress state evolution is linked to the progressive build up and interaction of gravitational loads between large shield volcanoes

Supporting Information:
- Supporting Information S1

Correspondence to:
S. Pierdominici,
pierdo@gfz-potsdam.de

Citation:
Pierdominici, S., Millett, J. M., Kück, J. K. M., Thomas, D., Jerram, D. A., & Planke, S., et al. (2020). Stress field interactions between overlapping shield volcanoes: Borehole breakout evidence from the island of Hawai'i, USA. *Journal of Geophysical Research: Solid Earth*, *125*, e2020JB019768. https://doi.org/10.1029/2020JB019768

Received 23 MAR 2020
Accepted 24 JUN 2020
Accepted article online 26 JUN 2020

Abstract Knowledge of the in situ stress state of the Earth's crust plays a key role in understanding geological processes including plate tectonics, earthquakes, slope failure, and igneous emplacement. In this paper, we determine the in situ stress orientation from the PTA2 borehole on the island of Hawai'i, drilled into a lava flow dominated sequence between Mauna Kea and Mauna Loa. High-resolution acoustic images were collected from the open hole interval 886 m to 1,567 m. Based on identification of 371 borehole breakouts for a total length of 310 m, the mean orientation of the minimum horizontal principal stress is N106° and remains constant across different volcanic rock fabrics. Changes in borehole breakout shape are linked to the different strength of volcanic facies and intra-facies. The orientation of the present-day stress field at Mauna Kea deviates from the plate forces and regional tectonic stress field. We interpret the compressive stress regime at the PTA2 site as resulting from the competing gravitational fields of the large topographic highs of Mauna Kea and Mauna Loa. Our study reveals that the mass accumulation associated with shield volcano growth imparts significant local variations to the subsurface stress state on volcanic islands consisting of overlapping shield volcanoes. The results have significant implications for stress accumulation leading to brittle failure and flank collapse, along with potentially influencing magma accumulation and ascent pathways during volcanic island evolution. This study provides the first insights into the orientation of the present-day stress field between the major island forming shield volcanoes of Hawai'i.

1. Introduction

The determination of the present-day stress field in the Earth's crust is fundamental for investigations of the mechanical behavior of rocks, fluid flow at depth, and in revealing mechanisms that cause tectonic plates to move, fault, or rupture (Amadei & Stephansson, 1997; Engelder, 1993; Zang & Stephansson, 2010; Zoback, 2007). In general, three orders of stress patterns are present in the Earth's crust: first order (plate tectonic scale), second order (regional scale), and third order (local scale) (Zoback, 1992). The third order (local scale) of stress patterns is controlled by basin geometry, topography, local inclusions, density contrasts, and active faults (Heidbach et al., 2007; Zoback, 1992) and can show significant deviations from regional and plate stress patterns (e.g., Bell, 1996a, 1996b; Pierdominici & Heidbach, 2012; Tingay et al., 2006). The present-day stress field is described by four main stress indicators: earthquake focal mechanisms, wellbore breakouts and drilling-induced fractures, in situ stress measurements (including over-coring, hydraulic fracturing, and borehole slotter), and young geologic data (from fault-slip analysis and volcanic vent alignments) (e.g., Heidbach et al., 2016).

The island of Hawai'i is located within the Pacific Ocean and comprises one of the best studied and monitored volcanoes on the planet (Barnard, 1995; Poland et al., 2018; Tilling et al., 2014). Available stress data for the island of Hawai'i are derived mainly from focal mechanism solutions of earthquakes and geological field analysis of recent faulting. These extensive data sets reveal the respective role of rift zone intrusions,

surface exposures, flank sliding/collapse, and lithospheric flexure mainly linked to the two active volcanoes Mauna Loa and Kīlauea (e.g., Borgia & Treves, 1992; Cannon et al., 2007; Klein, 2016; Le Corvec & Walter, 2009; McGovern, 2007; Moore et al., 1994). Volcanic lineaments and faulting on topographic ridges on Mauna Kea volcano are very poorly developed, with shield-stage rift zones overlain by post-shield volcanic strata (e.g., Cannon et al., 2007). In contrast to the extensive surface and deep seismic data sets, subsurface measurements documenting the stress state of the island of Hawai'i are restricted to the HSDP borehole, located near Hilo on the eastern flank of the island. To date no subsurface measurements have been presented from the central areas of the island, and therefore, the present-day stress field and the potential influences of the competing large shield volcanoes have remained unknown until now. Within this contribution, we determine the orientation of the present-day stress field from borehole analysis in the center of the island of Hawai'i between the large Mauna Loa and Mauna Kea shield volcanoes.

The Humu'ula Groundwater Research Project (HGRP) drilled two boreholes in order to obtain a complete data set of fully cored volcanic rocks with associated borehole measurements and to characterize the groundwater resources in the saddle region (Jerram et al., 2019). The PTA2 borehole was drilled in the saddle region between Mauna Kea and Mauna Loa and offers a unique opportunity to study the previously untested subsurface of central Hawai'i. Within this study, high-resolution borehole images acquired by an acoustic borehole imager are used to detect and interpret borehole breakout features which are utilized to reconstruct the present-day stress state in the borehole. We identify linkages between borehole breakout magnitude and different volcanic rock properties, including porosity and rock strength.

Our analysis provides the first subsurface evidence to suggest that the competing gravitational loads of two large overlapping shield volcanoes form the primary control on the orientation of the present-day stress field. The subsurface stress indicators from the PTA2 borehole on the island of Hawai'i show an orientation of maximum horizontal principal stress about north-south that differs from the northwest-southeast orientation of the large-scale Pacific plate stress field (Torsvik et al., 2017). Knowledge of the shallow stress field may impact future borehole planning and aquifer/geothermal resource management and may also give important information for understanding the influence of stress field evolution on ocean island development.

2. Geological and Tectonic Setting

The Hawaiian volcanic chain was created as the Pacific tectonic plate moved over the Hawaiian hotspot (Fiske & Jackson, 1972; Sherrod et al., 2007; Wilson, 1963; Figure 1a). Hawai'i Island's volcanoes are the most recent expression of this process that has created the 6,000 km long Hawaiian Ridge-Emperor Seamount chain over a period of about 70 million years (Appleman, 1987; Clague & Dalrymple, 1987; Sharp & Clague, 2006; Watson, 1999). The island of Hawai'i is the closest to the present-day mantle plume and consequently is a volcanically active region comprising the youngest part of the island (%3C0.4 Ma; Figure 1b). It is composed of five volcanoes on land, of which three (Kīlauea, Mauna Loa, and Hualālai) are still considered to be active. Offshore, the still growing Lō'ihi seamount is the only known pre-shield stage volcano in the chain. Mauna Kea is one of the five shield volcanoes on the island of Hawai'i, and it is in a dormant phase having last erupted approximately 4,000 ka (Porter, 1987).

Mauna Kea's subaerial edifice was formed in two main stages: first, a shield stage dominated by tholeiitic basalts was emplaced and, secondly, a post-shield stage with tholeiitic and alkali basalts (Frey et al., 1990, 1991; Wolfe et al., 1997). The post-shield lavas are subaerially exposed with two main lava units: (i) the tholeiitic, transitional-alkalic basalts of the Hāmākua volcanics (250–65 ka) (Frey et al., 1990, 1991; Wolfe et al., 1997) and (ii) Laupāhoehoe volcanics (66–4 ka). The latter include mainly hawaiite and less abundant mugearite and benmoreite (West et al., 1988; Wolfe et al., 1997) for the most recent volcanic flows (Frey et al., 1990). Volcanic lineaments on Mauna Kea are scattered and poorly developed or not present (Cannon et al., 2007; Sherrod et al., 2007). The shield stage rift zones of Mauna Kea are thought to be buried by the Mauna Kea post-shield volcanic lineaments (Cannon et al., 2007), and therefore, no fissure vents, open cracks, and normal faults along the rift zone axes are clearly present at the surface. The location and orientation of the Mauna Kea ridge is still debated (Figure 2) (Holcomb et al., 2000; Moore & Clague, 1992; Morgan et al., 2010; Peterson & Moore, 1987). However, recent geophysical surveys on Mauna Kea's east flank have shown evidence of a buried rift system (Park et al., 2009; Thomas, 2016). The

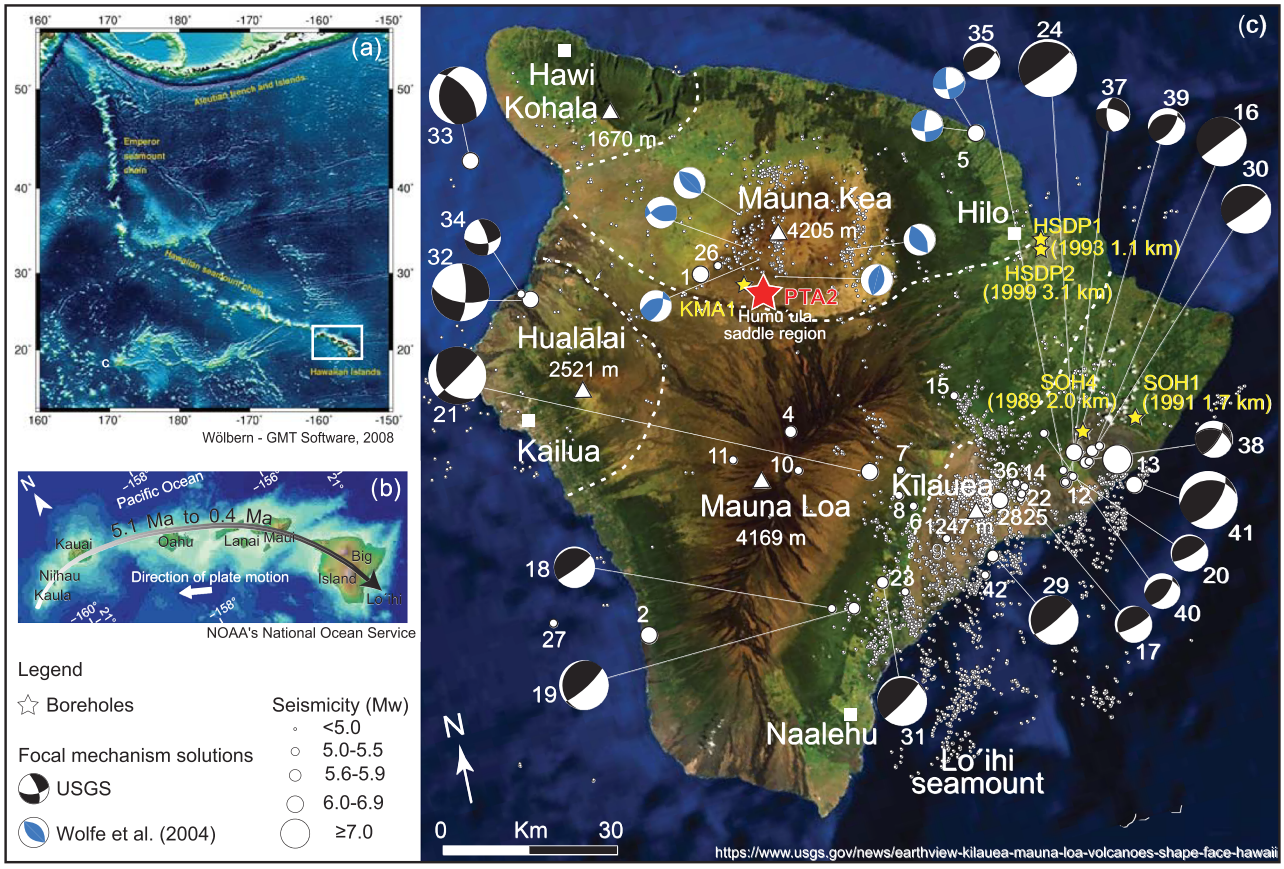

Figure 1. (a) 6,000 km long Emperor-Hawaiian seamounts chain of tholeiitic shield volcanoes. (b) The tectonic plate moves toward WNW building the oldest volcanic islands in the NW area of the island chain, and the recent expression of hot spot activity is to the SE of the island of Hawai'i (%3C0.4 Ma, Lō'ihi). (c) Island of Hawai'i. PTA2 (red star) and KMA1 boreholes (yellow star) have been drilled on the southwestern flank of Mauna Kea volcano. Yellow stars also show the locations of some other deep boreholes drilled on the eastern part of the island. In brackets, the year and the depth of drillings. Seismicity and the focal mechanism solutions are scaled according to the magnitude; the numbers for each event reference details for each event are presented in Table S1.

Mauna Kea volcano is also affected by a little seismic activity. The relocated earthquakes beneath Mauna Kea by Wolfe et al. (2004) show a hypocenter depth between 15 and 50 km with a prevailing compressive stress field and a radial distribution of P-axis orientation (Pritchard et al., 2007; Wolfe et al., 2004). In contrast the island of Hawai'i is dominated by strong and intense seismicity due to the Kīlauea and Mauna Loa active volcanoes. Forty-two earthquakes have been located at a depth greater than 5 km recorded by the National Earthquake Information Center from 1929 to 2018 with $M_w \geq 5.0$ (NEIC; https://earthquake.usgs.gov/contactus/golden/neic.php), which shows that the area is dominated by compressive and strike-slip regimes (Figure 1c; Table S1). The area shows variable P-axis azimuths with a preferred northwestern orientation in contrast with the orientation of maximum horizontal principal stress from the borehole analysis. Focal mechanism solutions show a complex system with a mixture of normal, strike-slip, and reverse faulting, reflecting the influence from both magmatic and tectonic activities. The P-axes azimuths show a southeast orientation close to the south flank of Kīlauea and to the southeast flank of Mauna Loa, a west orientation close to the summit zone of Mauna Loa, and in the strike orientation of the East Rift Zone at Kīlauea's summit caldera. The seismicity above 15 km is located under the caldera and active rift zones, and it is mainly related to dike emplacement and magmatic activity (e.g., Klein, 2016; Lin & Okubo, 2016, and reference therein). The deeper seismicity is mainly associated with flexure and subsidence under Mauna Kea and Mauna Loa volcano load (e.g., Klein & Koyanagi, 1989; Moore, 1970; Pritchard et al., 2007; Walcott, 1976; Wolfe et al., 2004). The complexity of the tectonic and volcanic setting of the island of Hawai'i, at different depths and at different volcanic centers, reflects the variability of stress and strain states (e.g., Klein, 2016; Lin & Okubo, 2016, and reference therein). In the

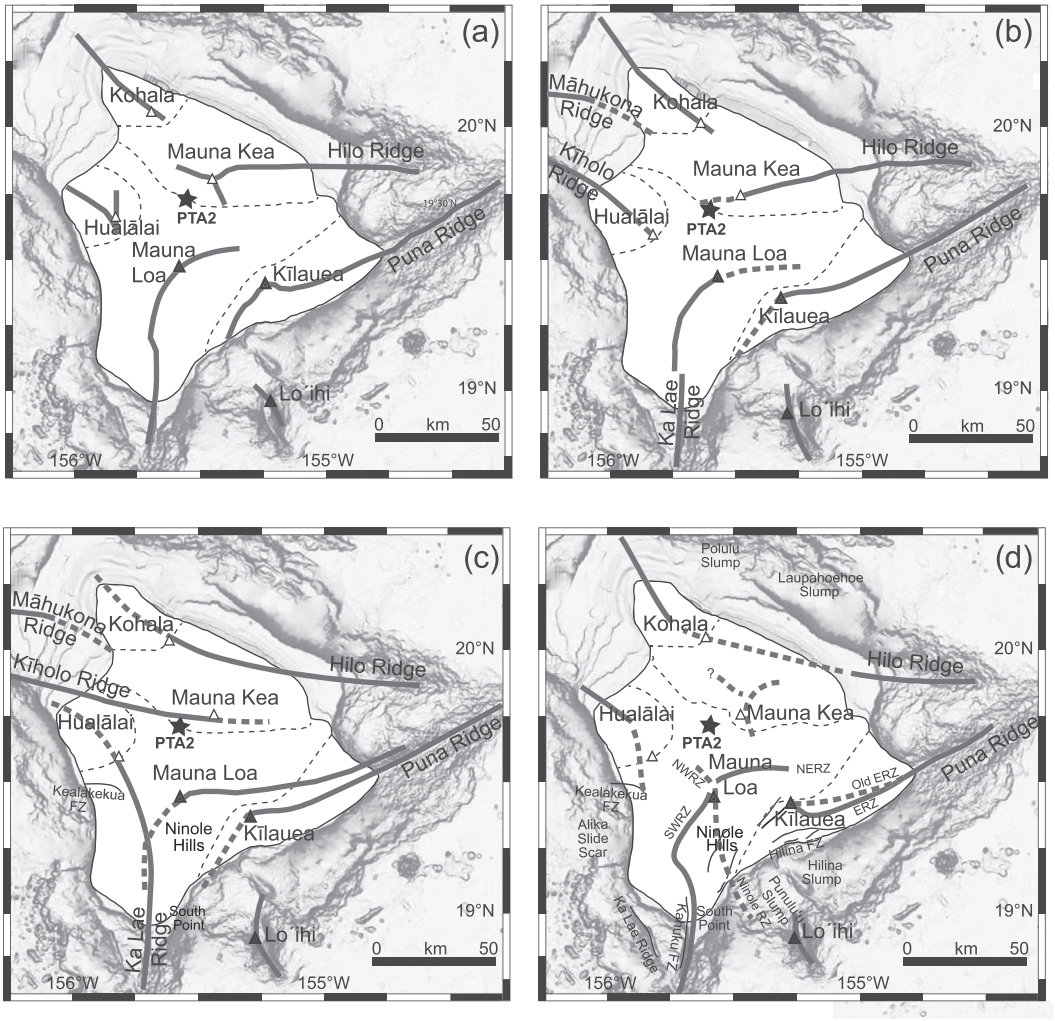

Figure 2. Four possible hypotheses of rift zone geometries of the island of Hawai'i. (a) Modified from Peterson and Moore (1987), Fornari (1987), and Moore and Chadwick (1995); (b) and (c) modified from Holcomb et al. (2000); (d) modified from Morgan et al. (2010). Legend: Active and buried rift zones in thick solid and dashed gray lines, respectively; the volcano boundaries in dashed black lines; exposed caldera in solid black triangle, inferred buried caldera in black and white triangle; black lines are the observed faults; location of PTA2 borehole in black star. SWRZ: Mauna Loa's southwest rift zone; NWRZ: Mauna Loa's northwest rift zone; ERZ: Kīlauea's east rift zone; FZ: fault zone; the bathymetry is from Eakins et al. (2003).

center part of the island of Hawai'i between Mauna Loa and Mauna Kea volcanoes, no seismic event has been recorded at shallow depths (see, e.g., Klein, 2016). Clear geological surface evidences for stress indicators are also lacking in this area (Cannon et al., 2007). The World Stress Map catalogue of the island of Hawai'i shows few focal mechanism solutions but again with none from the center of the island (see the inset of Figure 12a). The analysis of borehole breakouts from the PTA2 borehole within this study enables an appraisal of the present-day stress field at shallow depths within the center of the island of Hawai'i for the first time.

3. Drilling Activity on Island of Hawai'i

By the end of the twentieth century, several deep (1 km) borehole studies on the subsurface geology of the island of Hawai'i had been completed (Tilling et al., 2014). Between 1989 and 1991, three scientific boreholes (SOH 1, SOH 2, and SOH 4) were drilled into Kīlauea's Lower East Rift Zone (LERZ) reaching depths between 1,700 and 2,000 m. In 1993 a 1,056 m borehole and from 1999 to 2007 a 3,520 m borehole were

drilled as part of the Hawai'i Scientific Drilling Project (HSDP; see hawaii.icdp-online.org) partially funded by National Science Foundation of USA (NSF) and the International Continental Scientific Drilling Program (ICDP) with the main objective to characterize the chemistry of lavas generated by the mantle plume during Mauna Kea's evolution and to get information about the state of the stress field present within the volcanic shield. The borehole breakout analysis, performed in the deeper HSDP hole, allowed to determine a north-south and east-west orientation of maximum and minimum horizontal principal stresses (S_H and S_h), respectively (Morin & Wilkens, 2005).

More recently, the PTA2 borehole was drilled in Pōhakuloa Training Area (PTA) on the southwestern flank of the Mauna Kea volcano in 2013 within the Humu'ula saddle region, between the Mauna Kea and Mauna Loa volcanoes (see Figure 1c). PTA2 was drilled as part of the Humu'ula Groundwater Research Project (HGRP) with the primary objective of testing for groundwater resources potential. The PTA2 borehole provided a 1,794 m deep fully cored section through the volcanic sequence (Figure 3) revealing spectacular detail of the subaerial lava-dominated volcanic facies (Jerram et al., 2019). The PTA2 borehole sampled the shield stage strata (from approximately 300 m to the bottom) and the post-shield sequence, including Hamakua and Laupāhoehoe lavas (0 to approximately 300 m; Figure 3a). The stratigraphic section is dominated by basaltic lava deposits (including ‘a’ā, transitional, and pāhoehoe facies; HGRP website; Jerram et al., 2019) with subsidiary occurrences of ash, breccia, and volcanoclastic layers, as well as thick cinder deposites and some identified intrusive layers (Figure 3b).

A suite of downhole logging measurements in the PTA2 hole was performed in June 2016 by the Operational Support Group at GFZ German Research Centre for Geoscience (Jerram et al., 2019) and included total natural gamma ray, spectral gamma ray, magnetic susceptibility, sonic velocity, dipmeter with four-arm caliper, and the ABI43 acoustic borehole imager (Figure 3c). The downhole geophysical measurements provide a unique opportunity to measure and determine the in situ geophysical and structural properties of the Mauna Kea volcanic rocks. Downhole logging has investigated the open hole section between 886 and 1,567 m. Total natural gamma radiation was also measured in the cased upper hole section from 0 to 886 m. The lowermost section between 1,567 and 1,764 m was not accessible for wireline tools. All logs (except the acoustic image log) were depth synchronized by gamma ray correlation. The acoustic images were depth corrected by matching the caliper and the magnetic field intensity of the acoustic imager with those of the dipmeter tool (which beforehand was GR depth-matched).

4. Method: Acoustic Borehole Imaging

The measuring principle of an acoustic borehole imager (ABI) (Zemanek et al., 1969) consists of a piezo-electric acoustic transducer which emits an ultrasonic pulse (1.2 MHz) to the borehole wall where the pulse is being reflected and received by the same transducer. A rotating acoustic mirror in the beam path directs the pulse sequentially along the circumference covering the entire 360° of the borehole wall. The spatial orientations of tool and borehole are determined by built-in triaxial accelerometers and magnetometers. The acoustic borehole imager tool delivers two types of information:

a Acoustic two-way travel time (TT) is the time between transmission of the sonic pulse and reception of the reflected pulse at the transducer. The TT image yields information on the borehole shape (acoustic caliper).
b Acoustic amplitude (AMPL) delivers information on the acoustic reflectivity of the borehole wall resulting from the acoustic impedance contrast between borehole fluid and wall. The AMPL image depends on the roughness and shape of the borehole wall and its acoustic properties.

These TT and AMPL acoustic images are visualized in 360° images of the borehole wall versus depth and are presented in colors that code their value range. In the TT image, the bright colors indicate short time period (fast) for the impulse to go from the transducer and back to the receiver; the dark colors represent long time period (slow), which means widened size of the borehole. In the AMPL image, bright colors (high amplitude) indicate a strong signal (good reflection and strong contrast), and dark colors (low amplitude) indicate weak to missing signals (scattered or absorbed impulse). In both acoustic images, therefore, features such as open fractures, voids, washouts, and breakouts are in dark colors (low amplitude and slow travel time).

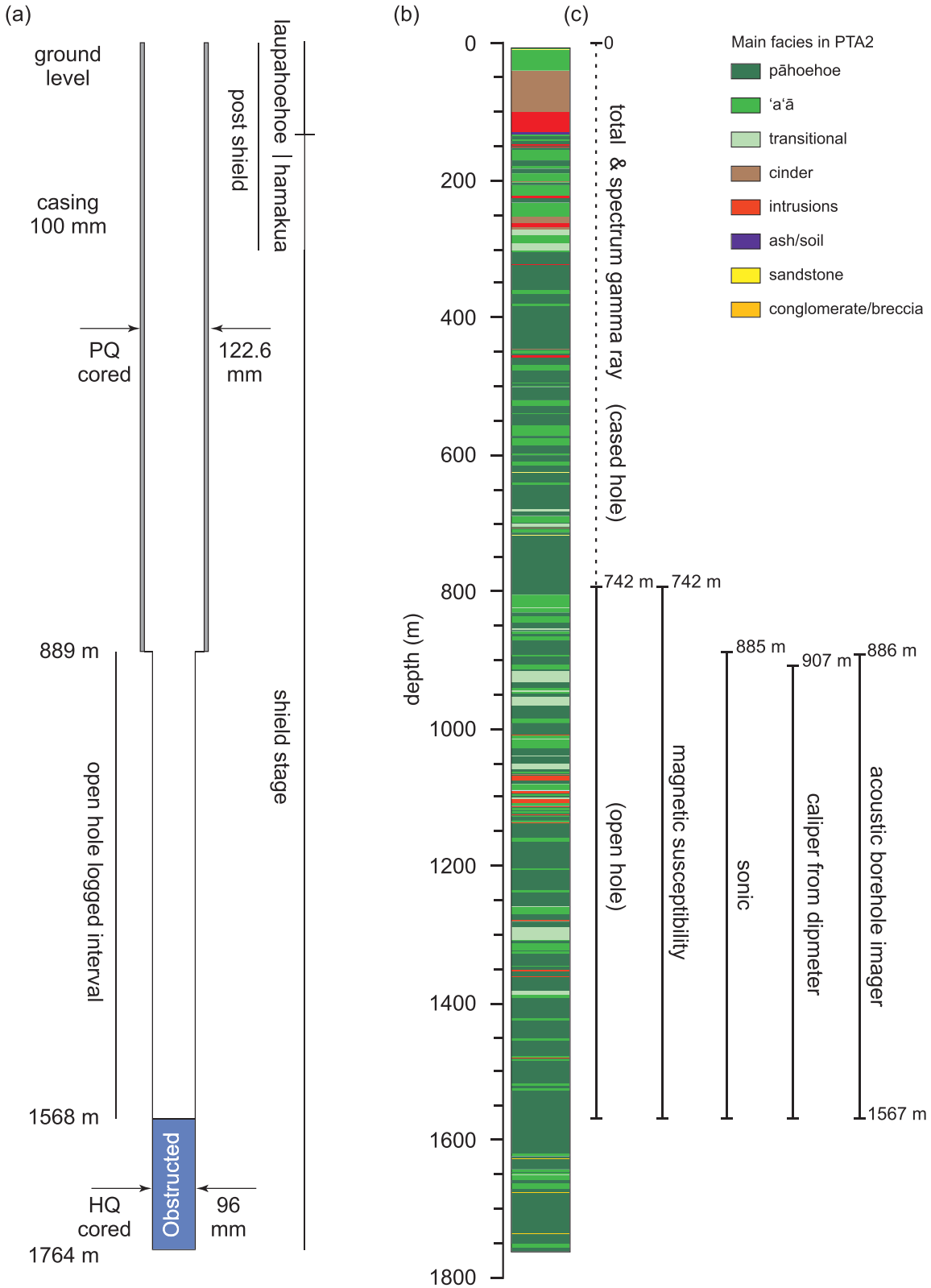

Figure 3. (a) Sketch of the PTA2 borehole. (b) Lithological profile (modified after Jerram et al., 2019). (c) Suite of downhole logging measured in 2016. Downhole measurements mostly investigated the open hole section between 886 and 1,567 m (solid black line), except total natural gamma ray that was also acquired from 0 to 886 m inside the casing (dashed black line).

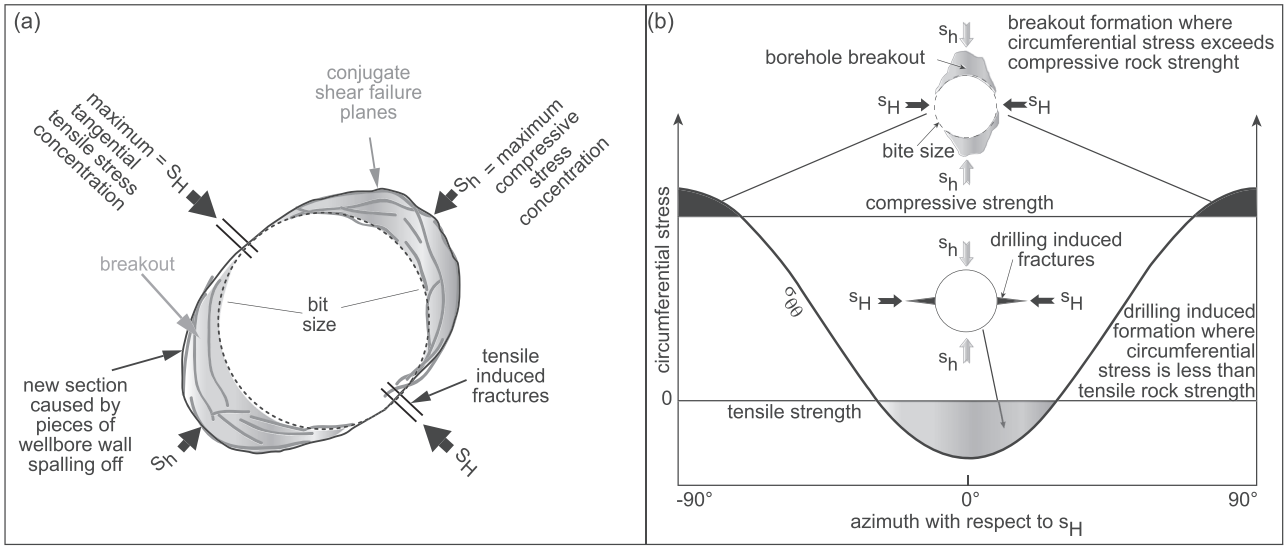

Figure 4. (a) Schematic figure showing the geometry of the induced drilling features on horizontal plane (modify from Bell & Gough, 1979). The breakout zones develop at diametrically opposing sides, and the main axis of the elliptical zone is parallel to the orientation of the minimum horizontal principal stress (S_h). Perpendicular to these features, induced tensile fractures can appear, and their orientation is parallel to the maximum horizontal principal stress (S_H). (b) Physical explanation of the development of borehole breakout and drilling induced fractures (modified from Hillis & Reynolds, 2000).

In this study, the ABI43 tool has been used (Table S2), and all recorded acoustic images have been oriented with respect to the magnetic north, filtered and edited for noise from the data records by interpolating the bad signals, scaled and calibrated for the borehole size (96 mm), and finally corrected where the tool was decentralized. These processing steps were necessary to avoid distortion, misinterpretation, and incorrect geometry (e.g., strike, dip, and width) of the features. The processing allows us to enhance data quality in order to recognize very small features that would otherwise have been overlooked. Image logs are a powerful tool to identify geological features such as thin beds, volcanic facies, sedimentary sequences, slumps, conglomerates, bedding planes, foliations, tectonic features, such as fractures and faults, and drilling-induced features as borehole breakouts and drilling-induced fractures. Here, we focus only on borehole breakout features identified and processed with the logging data software WellCAD5.1 ALT company (www.alt.lu).

4.1. Borehole Breakouts

When drilling a borehole into the Earth's crust, which is under a nonuniform in situ stress condition, rock failure can occur around the borehole where the stress exceeds the rock strength (Haimson & Herrick, 1985; Zang & Stephansson, 2010; Zoback et al., 1985). The zones of broken and spalled-off rock material in the wellbore walls generate bidirectional stress-induced borehole enlargements widely known as borehole breakouts (e.g., Babcock, 1978; Bell & Gough, 1979; Plumb & Hickman, 1985). The stress concentration around a vertical borehole, drilled parallel to the vertical principal stress (S_v), is described by the Kirsch equations (Kirsch, 1898). The maximum compressive stress on the borehole circumference occurs parallel to the minimum horizontal principal stress axis (S_h); the maximum tangential tensile stress occurs parallel to the maximum horizontal principal stress axis (S_H) (Figure 4a). Therefore, the borehole breakouts develop parallel to the S_h, because maximum compressive stress concentration is built up at the borehole wall in this direction (Figure 4a; Bell & Gough, 1979; Plumb & Hickman, 1985; Zoback et al., 1985).

Borehole breakout enlargements form due to compressive shear failure of the borehole wall, which generates shear yield, destroying cohesion and weakening the rock (Bell & Gough, 1979). Intersecting conjugate shear planes develop, ultimately causing pieces of the borehole wall to spall off (Figure 4; Bell & Gough, 1979). The determination of borehole breakouts, together with other features (such as natural and drilling-induced fractures), and their spatial distribution, frequency, and orientation are fundamental for reconstructing the present-day stress field. In acoustic image logs in subvertical wells (%3C10° deviation), borehole breakouts appear with low AMPLs and slow TTs and hence show as pair of dark stripes on

opposing sides of the wellbore wall (Figure 4a). Borehole breakouts bridge the gap between near-surface stress indicators from geological data and deep stress indicators from earthquake focal mechanisms at greater depth (Zoback et al., 1989). The present-day stress field orientation by borehole breakouts forms an essential part of the World Stress Map Project (WSM; Heidbach et al., 2018; Zoback, 1992). The borehole breakouts contribute approximately 20% of the WSM database, and their contribution is growing (Heidbach et al., 2016; Tingay et al., 2006).

4.2. Quality Data Control: Artifacts in the Image Log

High-resolution image logs also display some features related to drilling operations such as vertical drag lines, drill bit marks, stick and pull zones, and horizontal striping (e.g., García-Carballido et al., 2010; Lofts & Bourke, 1999). These features can alter the image quality (signal to noise ratio) and lead to misinterpretations. The PTA2 acoustic images contain drilling-induced artifacts. These artifacts arise from mechanical wear during drilling, tripping, and back-reaming activities. These superficial marks are visible especially in the upper part of the wellbore due to the frequent round trips (Figure 5a). Subvertical scratches appearing also in the image log are interpreted as drilling-caused marks induced by moving of the drill string (Figure 5b).

The image log is affected in some zones by measurement artifacts such as horizontal striping due to momentary interruptions of data acquisition reducing the quality of the image, especially in the uppermost and lowermost sections of the image log (Figure 5c). The first class of artifacts of the PTA2 image log, which are most common, is the so-called "stick and pull zones" (Lofts & Bourke, 1999). The presence of stick and pull zones reduces the image quality of the log and arise from drag effects acting on upward tool travel.

Even if stress-induced structures would be present, they would be concealed and blurred making them extremely difficult to identify, classify, and measure. The tool sticking is also easily identified from the acceleration curve where the frequency and the amplitude significantly change (gray curve in Figure 5d). The second group includes the borehole wall artifacts, which are caused by irregularities in the wellbore such as roughness, mud cake, spiral hole, and washout (Figure 5e).

5. Results of Borehole Breakout Analysis

5.1. Borehole Breakout Orientation

The ABI interval was logged from 886 to 1,567 m (Figure 3c), and a total of 371 borehole breakouts was identified in the acoustic images (Figure 6). The breakouts occur in 310 m of the 681 m long logged section (Figures 7a and 7b) representing 45% of the entire section (Figure 8a). The analysis exhibits a constant azimuth of S_h mean = 105.9° (st.dev. = 13°) along the entire logged interval crossing all lithological units with no change in orientation (Figure 7 and Tables S3 and S4).

The borehole breakouts have been divided into two groups. Borehole breakouts with high confidence and well-defined extent are assigned a good quality (Q = 1) and defined as major breakouts. Borehole breakouts with lower confidence have been ranked as poor quality (Q = 2) and called minor breakouts. The Q2 group includes breakouts with small size in width, length, and depth and also includes poorly developed examples termed "incipient-breakouts." The distribution of these two groups has been analyzed for cumulative lengths and number versus the borehole lithology (Figure 8). One hundred and forty-seven Q1 borehole breakouts (brown dots in Figure 7d) with a cumulative length of 123.15 m were recognized representing approximately 18% of the entire logged interval (Figure 8a). Most of Q1 breakouts are focused in pāhoehoe and 'a'ā lavas and in the intrusion intervals (Figure 8). Two hundred and twenty-four Q2 borehole breakouts (blue dots in Figure 7d) have been distinguished with a cumulative length of 187 m (Figure 7d). The Q2 breakouts represent about 27.5% of the entire logged interval (Figure 8a), and they are developed dominantly within pāhoehoe lava facies (Figure 8b).

5.2. Borehole Breakout Geometry

The analysis of the horizontal cross-sectional shape of the borehole breakout shows different geometries of wellbore failures. The borehole breakout shapes were categorized in four groups based on their degree of symmetry (symmetric implies breakouts are 180° apart), width, and depth of the breakouts (Figure 9a; Sahara et al., 2014):

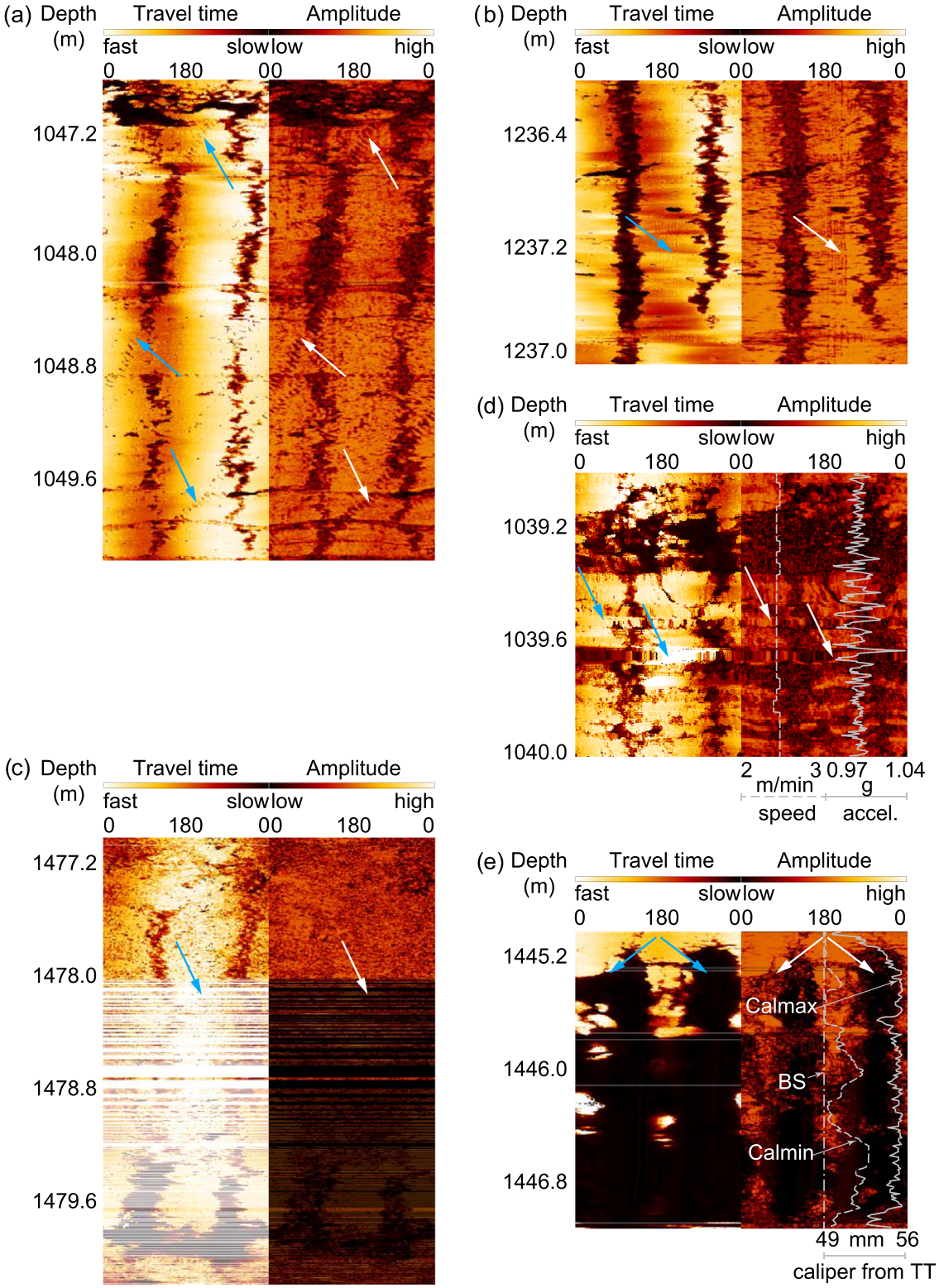

Figure 5. Types of artifacts observed on the acoustic image log. Drilling operation artifacts: (a) drill bit marks; (b) subvertical mechanical scratches. Acquisition artifacts: (c) horizontal striping; (d) stick and pull zones with related curves of acceleration and logging speed. Artifacts also arise from unfortunate borehole conditions: (e) extremely large zone with calipers clearly larger than bit size ($Cal_{max} \approx Cal_{min}$ %3E%3E BS). Blue and white arrows indicate the artifacts on transit time and amplitude image logs, respectively. Legend: Cal_{max}: caliper maximum; Cal_{min}: caliper minimum; BS: bit size; accel.: acceleration; TT: travel time.

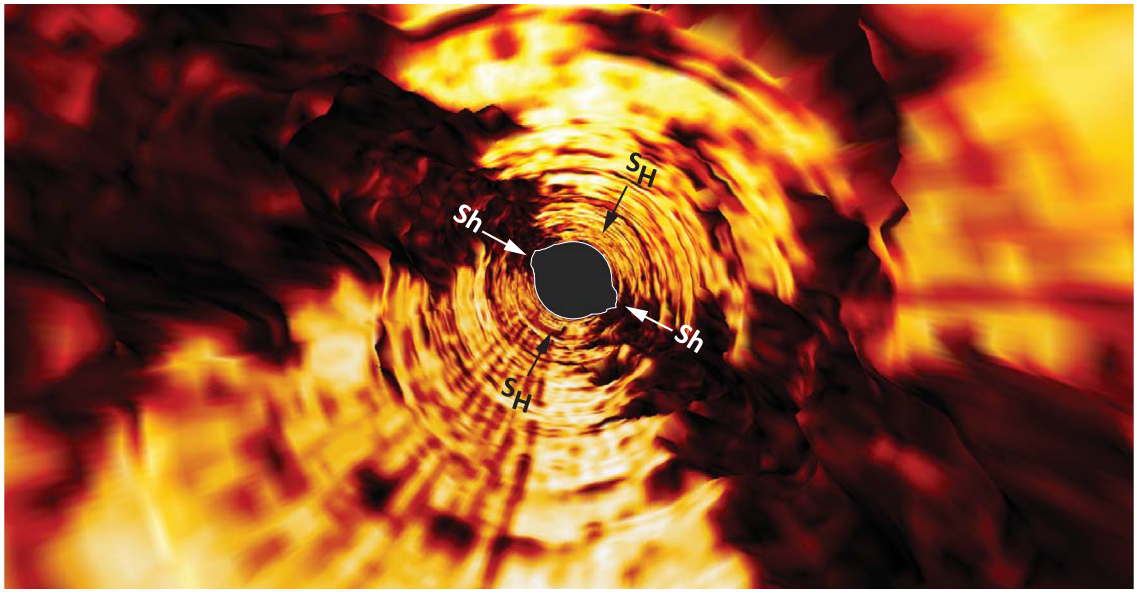

Figure 6. Three-dimensional borehole breakout view from ABI image of the PTA2 borehole wall. S_h and S_H are the orientations of the minimum and maximum horizontal principal stresses, respectively.

I Borehole breakouts occur as a paired enlargements having similar width ($\theta_1 = \theta_2$) and depth ($d_1 = d_2$) on opposite sides of the circumference (symmetrical).
II Borehole breakouts occur as a paired enlargements having similar width ($\theta_1 = \theta_2$) and depth ($d_1 = d_2$) but with asymmetrical orientation (not on opposite sides of the circumference).
III Borehole breakouts occur as symmetrical paired enlargements but have dissimilar width ($\theta_1 \neq \theta_2$) and/or depth ($d_1 \neq d_2$).
IV Borehole breakouts occur as very different developed paired enlargements having strongly dissimilar width (θ_1 %3E%3E θ_2) and/or depth (d_1 %3E%3E d_2) but are symmetrically oriented.

The analysis of the acoustic image of PTA2 wellbore reveals that the breakouts geometry (orientation, width, and depth) can occasionally take different shapes (Figure 9b). Most of the borehole breakouts show a symmetrical shape, and they have very good development in depth and width (Figure 9b (v)). The asymmetric breakout shapes are shown in Figure 9b (vi–viii). Some breakouts display slightly different orientation of one side of the breakout shifted by α (orientation of $S_{h1} \neq$ orientation of S_{h2}) in combination with different borehole breakouts widths (θ_2 %3E%3E θ_1; Figure 9b (vi)); other zones exhibit dissimilar breakout shape in width (θ_2 %3E θ_1) and depth of elongation ($d_1 \neq d_2$) as in Figure 9b (vii) and, finally, only an initial borehole breakout formation on one side of the borehole (Figure 9b (viii)).

In addition, in Figure 9b, we compare the breakouts identified in the AMPL image with the acoustic caliper (Cal_{min}, Cal_{max}) calculated from the TT and the two calipers measured by the four-arm caliper tool Cal C_1 and Cal C_2. The latter is useful for the identification of breakout when the diameter difference exceeds the bit size by more than 10% (Plumb & Hickman, 1985; Reinecker et al., 2016). The four-arm caliper tool cannot detect enlargements when the radial extension of the breakout is poorly developed into the formation (Figure 9b (vi)) and when the enlargements are only in incipient stage (Figure 9b (viii)). In both figures, the calipers Cal C_1 and Cal C_2 show the same size of the borehole diameter (bit size). Therefore, the number of borehole breakouts would be significantly lower than that detected by the acoustic borehole imager tool. Small rotations observed along the wellbore likely are related to the local variation in stress due to different rheology of the rocks linked to the rock strength.

The acoustic image analysis has also shown different stages of borehole breakout evolution. The first stage in the breakout formation starts by initiation of subvertical thin fractures (Figure 10a) because the already failed rock material has not yet spalled off from the borehole wall. Such features, called incipient-breakout, could be misinterpreted as drilling induced fractures; therefore, special attention was taken to identify them. The azimuth of these incipient borehole breakouts is consistent with the azimuth of the well-developed

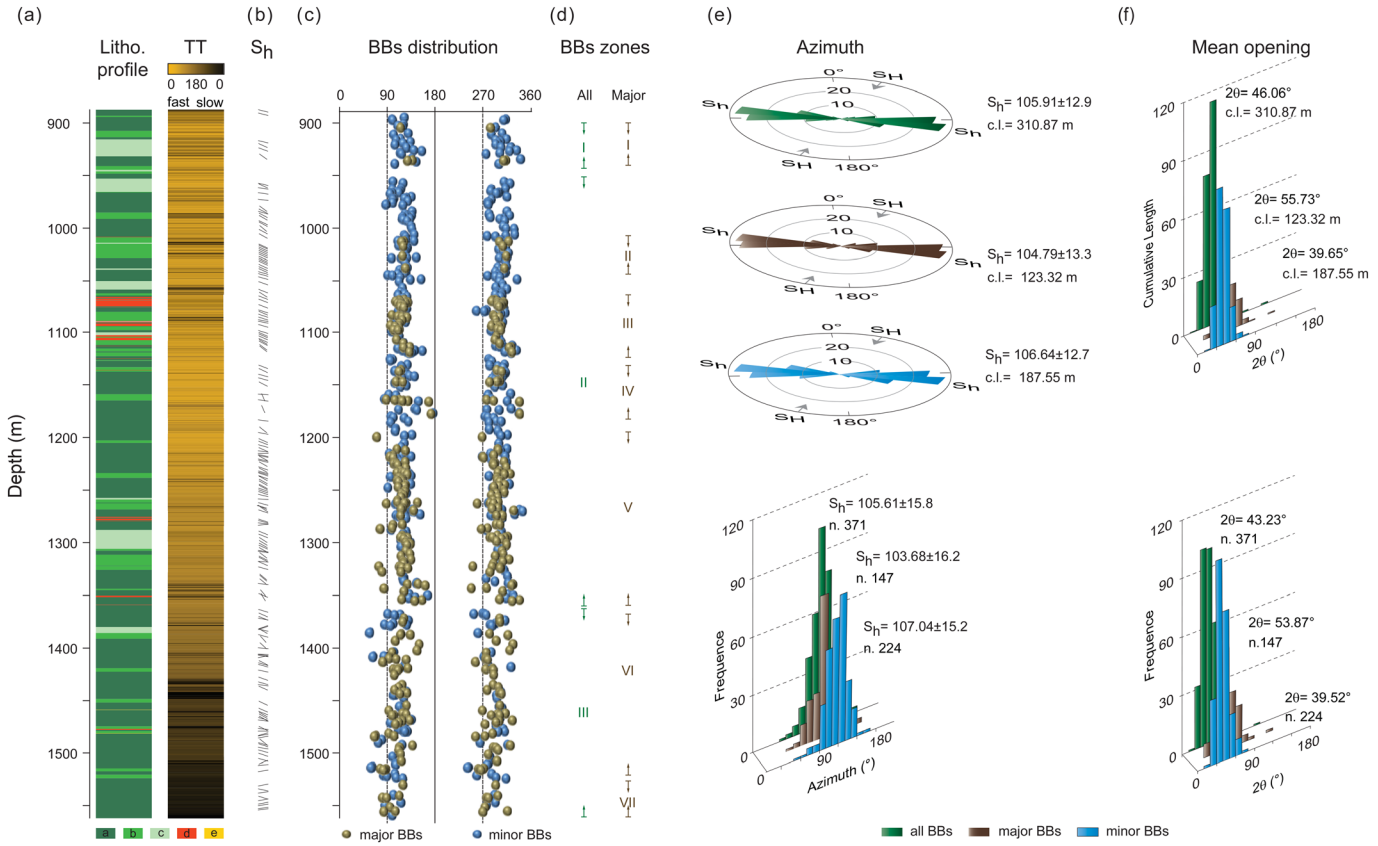

Figure 7. Breakout analysis: (a) lithology of the PTA2 borehole and travel time (TT) of the ABI43 tool; (b) distribution of the breakout orientation; (c) borehole breakout (BB) distributions; different colors indicate the quality of breakouts (major borehole breakouts Q1 in brown, minor borehole breakouts Q2 in blue); (d) Breakout zones recognized in the major breakouts and in the entire data sets; (e) rose diagrams of the S_h orientation from breakout orientation (all borehole breakouts = green, Q1 borehole breakouts = brown, Q2 borehole breakouts = blue) with associated standard deviation and cumulative length (c.l.), the plot below shows the borehole breakout azimuth distribution versus borehole breakout frequency (*n*: number of breakouts); (f) borehole breakout opening (2θ) versus cumulative borehole breakout length (above) and versus borehole breakout frequency (below). Legend of the main volcanic facies (modified after Jerram et al., 2019): a: pāhoehoe; b: 'a'ā; c: transitional; d: intrusions; e: conglomerate/breccia.

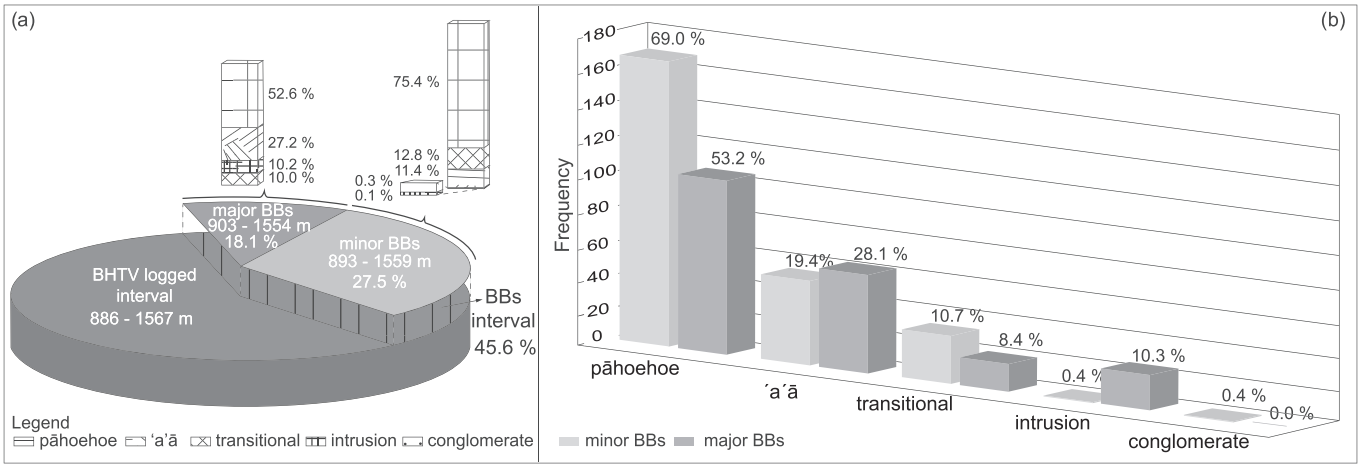

Figure 8. (a) Pie chart showing the distribution of minor (light gray color) and major (gray color) breakouts respect to the total ABI logged interval (entire pie, dark gray color) and (b) frequency of major and minor borehole breakouts per each main volcanic facies of PTA2 borehole.

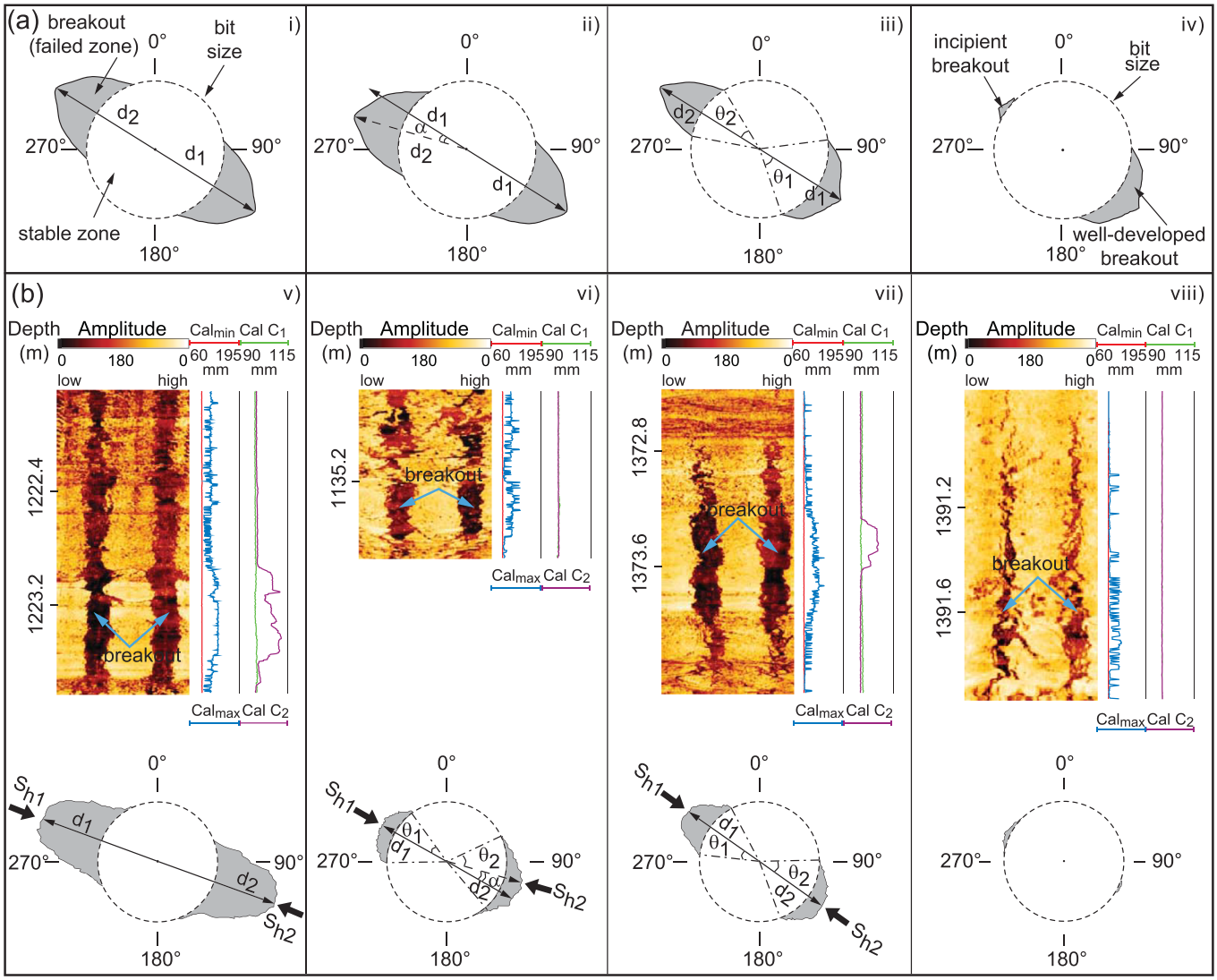

Figure 9. Breakout shapes: (a) text book examples of several types of breakout shapes in horizontal cross sections: (i) symmetrical shape with a symmetrical pair of similar deep ($d_1 = d_2$) extended and shaped "breakout-ears" on opposite sites (orientation S_{h1} = orientation S_{h2}); (ii) the breakout-ear on one side is not parallel with the opposite side's borehole breakout-ear direction but shifted by an angle α (orientation $S_{h1} \neq$ orientation S_{h2}); (iii) asymmetric shape of the two borehole breakout-ear with different breakout widths (θ_1 %3E θ_2) and/or with different extension depth ($d_1 \neq d_2$); (iv) well-developed breakout on one side and absent and/or only initially staged borehole breakout on the opposite side (θ_1 %3E%3E θ_2 and/or d_1 %3E%3E d_2). Combination of these four different features can also take place. Gray area shows the breakouts (zones of rock failure and spall off); the dashed line is the bit size of the borehole. (b) The above mentioned examples of breakout shapes in horizontal cross sections have been identified in the acoustic image logs of the PTA2 borehole. Cal$_{min}$ and Cal$_{max}$ = acoustic borehole calipers from TT image log (blue and red, respectively), Cal C$_1$ and Cal C$_2$ = mechanical calipers from four-arm caliper tool (green and purple, respectively); (v) good example of breakout development; (vi) different orientation and width (θ_2 %3E%3E θ_1); (vii) different width (θ_2 %3E θ_1) and depth of elongation ($d_1 \neq d_2$); (viii) unequal initial borehole breakout formation, where the western side is more developed than the other in both the amplitude image and cross section.

borehole breakouts (Barton & Moos, 2010; Trice, 1999). The cross sections (Figures 10a–10c) are still almost circular although in the travel time and amplitude image logs, the incipient breakouts are present (Figures 9a and 9b). Over time, more fractures will form, propagate, and merge causing chips of rock to spall off and develop into borehole breakouts, eventually also showing the typical borehole breakout cross section (Figures 10e and 10f).

5.3. Borehole Breakout Volcanic Facies Dependence

Borehole breakout shapes are related to rock type and are affected by range of different shapes (Figures 9 and 10). Within intervals of uniform facies, more mature borehole breakout development is often observed

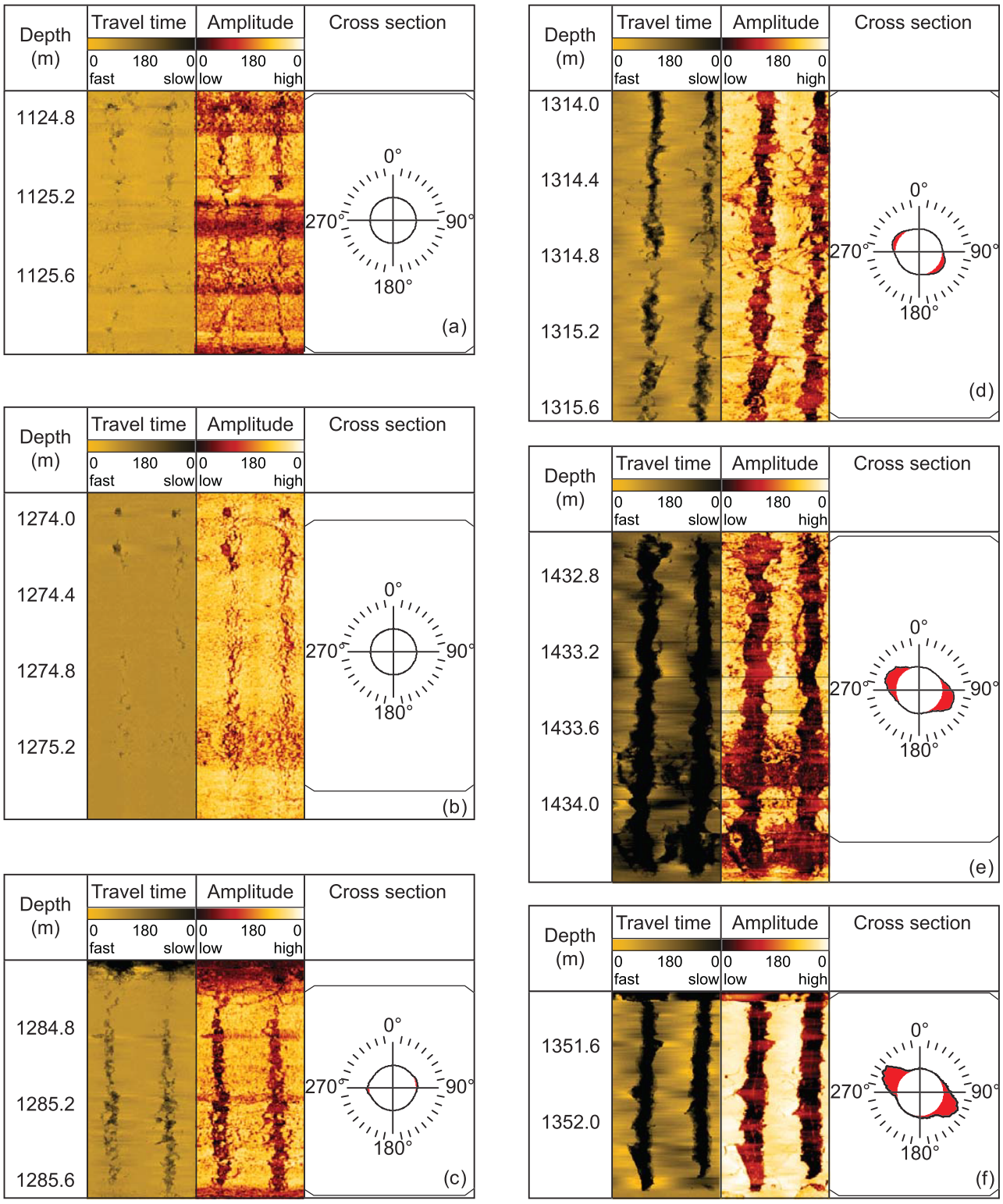

Figure 10. Snapshots from different development stages of borehole breakouts. (a) The first stage in the borehole breakout formation starts by initiation of vertical structures with almost similar appearance as drilling-induced fractures. The many micro fractures propagate and merge and hence chips of the rock begin to spall off the wall (c and d). The cross sections in (a) and (b) are still almost circular, although in travel time and amplitude images, the incipient breakouts are already visible. In time, more portion of rocks spall off the borehole wall, and the breakouts get more developed and ultimately show the typical almost oval "circle-with-ears" shape in the cross section (e and f).

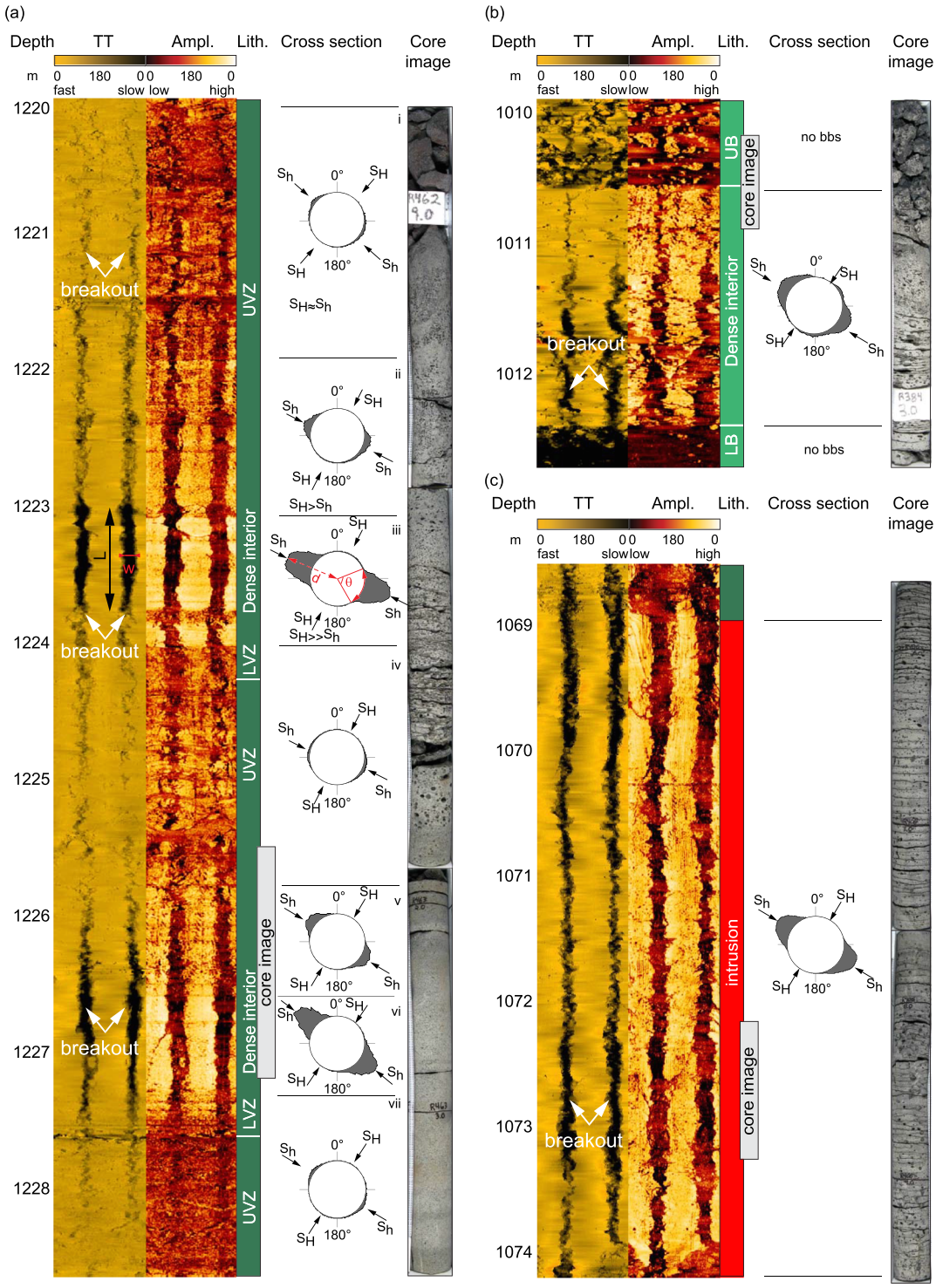

Figure 11. Borehole breakout volcanic facies dependence. (a) Different shapes of breakouts within a pāhoehoe facies layer (dark green color): incipient (i, iv, and vii), intermediate (ii and v), and mature stages (iii, and vi). The borehole breakouts at incipient and intermediate stages develop into upper or lower vesicular zones (UVZ and LVZ, respectively) of the pāhoehoe lava flows. The borehole breakouts at mature stage develop in the lower vesicularity and fresher dense interior zone of the pāhoehoe lava flows. Borehole breakouts at mature stage develop in the dense interior of the 'a'ā lava facies (b) and into the intrusion interval (c). The borehole breakouts are well-developed in the intervals with high amplitude images. Incipient borehole breakouts are mainly related to the low amplitude image log, which is linked to a combination of higher vesicularity, alteration, and fracturing. Selected core images reveal key elements of the different PTA2 facies examples. Core images show examples for core lava units in PTA2 borehole. Legend: TT: travel time; Ampl: amplitude; Lith.: lithology; L: length of the breakout; W: width of the breakout; d: depth of the breakout in the rock formation; UB and LB: upper and lower breccia, respectively.

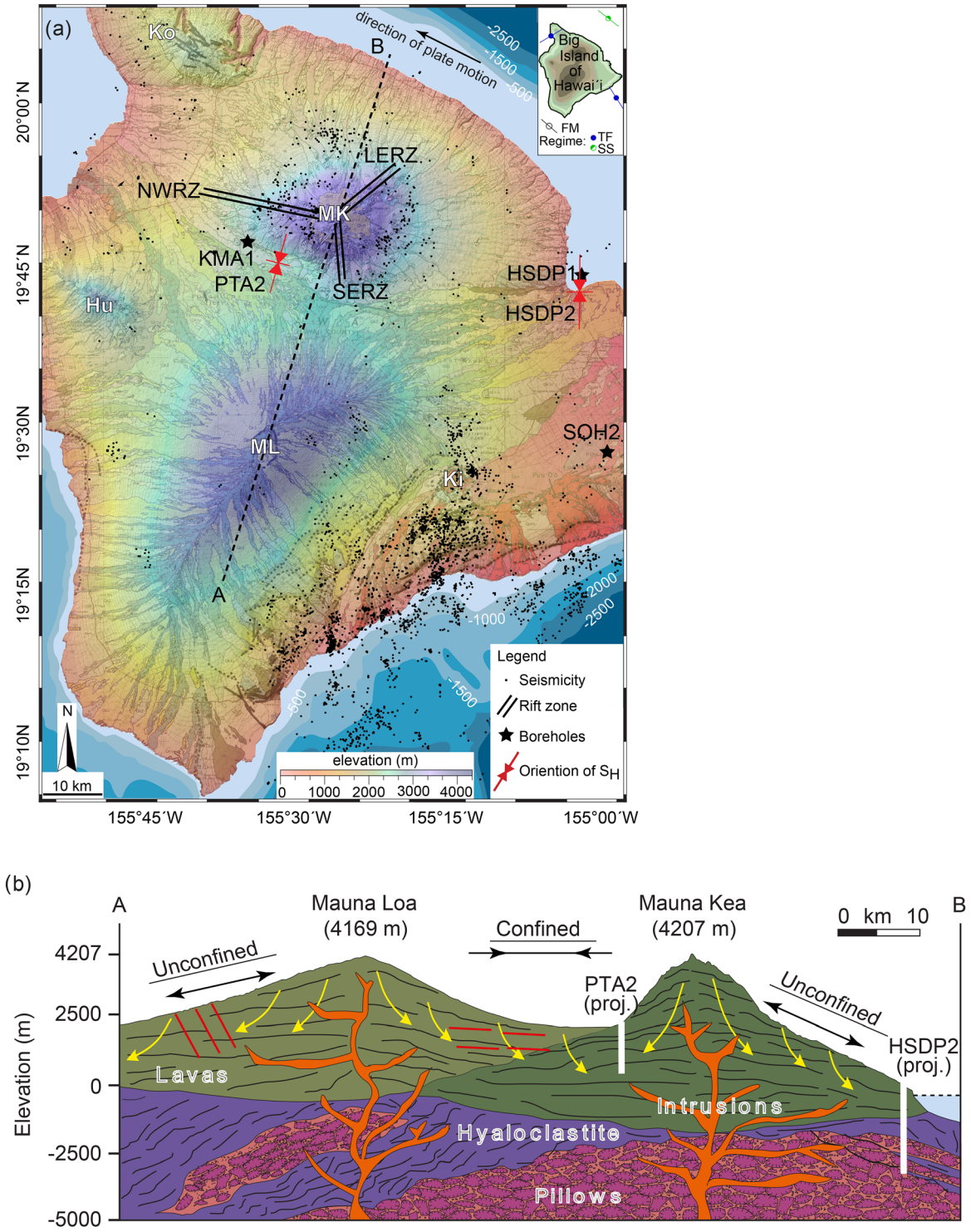

Figure 12. (a) Geological, elevation, and bathymetric map of Mauna Kea with elevations and depths in meters including: three rift zones (LERZ: east rift zone; NWRZ: northwest rift zone; SERZ: southeast rift zone); S_H orientation (in red) of PTA2 borehole from this study and from the HSDP2 borehole near Hilo (Morin & Wilkens, 2005); A–B is the trace of topographic profile (dashed line); the black dots represent the seismicity from 1929 to 2018 (NEIC; https://earthquake.usgs.gov/contactus/golden/neic.php); the 10-m digital elevation model of the island of Hawai'i (https://gis.ess.washington.edu/data/raster/tenmeter/hawaii/); geological map of the island of Hawai'i by Sherrod et al. (2007) and Wolfe and Morris (1996); the bathymetric map and the contour line of the topography are modified from Garcia et al. (2007); the inset shows the focal mechanisms (FM) as the only stress indicators (TF: thrust faulting and SS: strike-slip faulting) available in the World Stress Map (Heidbach et al., 2016). Legend: Hu: Hualalai, Ki: Kīlauea, Ko: Kohala, MK: Mauna Kea and ML: Mauna Loa. (b) Topographic profile of Mauna Kea and Mauna Loa shield volcanoes. PTA2 and HSDP2 boreholes are projected.

within the strongest intra-facies such as lava flow interiors (Figure 11). Within intervals having uniform facies, more mature development (e.g., more prominent enlargement in radial depth, greater width, or length of the enlargement) of the borehole breakouts appear to correspond to intra-facies intervals with greater strength (freshest and higher Vp) and density (lower porosity) such as the interiors of lava flow facies and intrusions (Figure 11). In the representative pāhoehoe facies example, the breakout shape evolves from an incipient stage (Figure 11a; 1,220.0–1,221.9 m (i), 1,224.0–1,225.7 m (iv), and 1,227.4–1,128.5 m (vii)) to a juvenile step (Figure 11a; 1,221.9–1,223.0 m (ii) and 1,225.7–1,226.5 m (v)) until it reaches the mature stage (Figure 11a; 1,223.0–1,224.0 m (iii) and 1,226.5–1,227.4 m (vi)). The three stages of breakouts reflect the different physical properties of the pāhoehoe lava. Less evolved breakouts appear only in zones where the pāhoehoe lava has a vesicular texture, as shown in the amplitude image and confirmed from core (low amplitude values; Figure 11a (i), (iv), and (vii)). In contrast, mature breakout stages are present in layers with high amplitude values in the image log indicating that it corresponds with the dense inner part of the lava flow (Figure 11a (iii) and (vi)).

Similar development stages are identified in ‘a’ā and sheet intrusion facies. In the ‘a’ā lavas, breakouts are best developed in intervals with high contrast in the amplitude (Figure 11b). In contrast, the enlargements are not present or very poorly developed in the ‘a’ā intra-facies with less contrast in the amplitude image (Figure 11b). Enlargements linked with the sheet intrusions which are characterized by extremely high impedance values and are prominent and very well shaped, (e.g., Figure 11c).

6. Interpretation and Discussion

The present-day stress field inside the island of Hawai'i likely results from the interference between several contributors happening at different depths: plate tectonic forces, lithospheric flexure, topographic loading, density contrasts, magma emplacement, and edifice deformation and failure (e.g., Fiske & Jackson, 1972; Le Corvec & McGovern, 2018; McGuire & Pullen,1989; Pritchard et al., 2007). Most commonly, only surface stresses constrained by neotectonics indicators and deep stresses constrained by focal mechanisms are investigated (NEIC, Wolfe et al., 2004).

The main orientation of the present-day stress field recorded on the island of Hawai'i shows high variability. The orientation of the P-axis azimuths indicates a complex system dominated by normal, strike-slip, and reverse faulting. This system is associated with the influence of both magmatic and tectonic activities (e.g., Klein, 2016; Lin & Okubo, 2016 and reference therein) and with flexure and subsidence under Mauna Kea and Mauna Loa volcano load (e.g., Klein & Koyanagi, 1989; Moore, 1970; Pritchard et al., 2007; Walcott, 1976; Wolfe et al., 2004). Within the central part of the island of Hawai'i, however, determining the present-day stress state is more challenging, because geological and tectonic surface structures are poorly visible and seismicity is dominantly located at depths greater than 15 km around Mauna Kea (Figure 1c, Wolfe et al., 2004).

Borehole breakouts within PTA2 therefore represent a unique opportunity for constraining the present-day stress states in the central part of the island of Hawai'i (Millett et al., 2018; Morin & Wilkens, 2005). The borehole breakouts observed in the acoustic image log indicate an orientation of the minimum (S_h) and maximum (S_H) horizontal principal stresses of N106° and N16°, respectively. These orientations remain consistent throughout the 681 m of open hole, showing that the measured stress orientation is robust and acts throughout a significant section of the upper crust in this area. In the broad scale, this orientation is rotated 100° from that of the Pacific Plate (Torsvik et al., 2017). However, it is known that active stress orientations measured in other parts on the island of Hawai'i also differ locally, as documented by the active rift zones (Figures 2 and 12a). For instance, (1) S_h is nearly oriented N-S in the eastern rift zone of Kīlauea (e.g., Wolfe et al., 2004), whereas (2) S_h is oriented NNW-SSE and WNW-ESE on the northeastern and southern rift zones, respectively, of Mauna Loa volcano as documented mainly by focal mechanism solutions and orientations of the dike emplacement (Klein, 2016; Walter & Amelung, 2006, and reference therein; Wolfe et al., 2004). Such complex stress orientation pattern strongly suggests that the stress orientation measured from borehole breakouts within PTA2 results dominantly from local effects.

A key observation is that the orientation of the maximum horizontal principal stress S_H measured within PTA2, which is located on the SW flank of Mauna Kea volcano, is parallel to an axis linking the summits

of Mauna Loa and Mauna Kea (Figure 12b). Both volcanoes exhibit substantial topography (4,207 m for Mauna Kea and 4,169 m for Mauna Loa). It is well known that topography and its compensation at depth can produce significant stress perturbations away from simple burial and tectonic stresses (Artyushkov, 1973; Hergert et al., 2015; Liu & Zoback, 1992; McGuire & Pullen, 1989). The local gravitational stresses associated with a high conical edifice can produce radial S_H stress trajectories, which can overprint the regional stress regime (e.g., Acocella & Neri, 2009; Chadwick & Dieterich, 1995; Delcamp et al., 2008; Dieterich, 1988; Kervyn et al., 2009; McGuire & Pullen, 1989). The stress orientation measured within the PTA2 borehole is consistent with the interference between the gravitational stress fields induced by the two large volcanic loads, which essentially restrict or buttress each other, leading to a focusing of compressional stresses in the saddle region. Similar scenarios have been modeled for irregular topographic loading in nonvolcanic settings (Pan et al., 1995). How these stress states evolve with greater burial and at what point they become aligned to the more regional stress field remains a subject for future modeling. What is clear here is that the stress state in areas comprising multiple major volcanic edifices in close proximity to each other will have a significant influence on the shallow stress state, which may influence edifice stability and shallow magma emplacement (e.g., Galland et al., 2018; Kervyn et al., 2009; Le Corvec & McGovern, 2018).

The stress orientation measured within the PTA2 borehole is very similar to that measured within the HSDP deep hole, which comprised the first determination of the present-day stress field orientation on the island of Hawai'i by breakout analysis in the late '90s (Morin & Wilkens, 2005). In this borehole, located far east of Mauna Kea volcano and north of Kīlauea Volcano, Morin and Wilkens (2005) revealed that the S_h and S_H are also orientated east-west and north-south, respectively. We argue that such orientation similarity between the stress fields estimated in PTA2 and HSDP is not related to a regional trend but instead relate to separate mechanisms. Morin and Wilkens (2005) interpreted the orientation of the stress field in the HSDP borehole as a consequence of the combination of increased north-south stresses due to the emergence of the Kīlauea Volcano and reduced east-west stresses due to gravitational instabilities in the onshore and offshore slopes of Mauna Kea volcano. Thus, even if stress orientations measured in PTA2 and HSDP are very similar, they likely result from very distinct origins.

It is well known that local stresses due to topographic loads have first-order effects on magma propagation through the crust (Galland et al., 2018; Hyndman & Alt, 1987; Kervyn et al., 2009; Muller et al., 2001, and references therein). Based on the observed present-day stress state at the PTA2 borehole, shallow dike emplacement would be expected to be dominantly parallel to an axis between Mauna Loa and Mauna Kea. However, an important condition is that Mauna Kea and Mauna Loa volcanoes did not build up at the same time. The topographic load associated with Mauna Loa has become progressively stronger as the edifice built up. Therefore, the stress states in the central part of the island of Hawai'i must have significantly evolved through time: A first state of stress due to the gravitational load of older Mauna Kea has likely been progressively affected/rotated by the growth of the younger Mauna Loa volcano. Thus, the timing of volcanic edifice buildup is crucial for interpreting the structure of paleo-rift systems and dyke swarms and vice versa. For instance, previous studies have identified a region of positive gravimetric anomaly (Flanigan & Long, 1987; Flinders et al., 2013) between Mauna Kea and Mauna Loa volcanoes, interpreted as an east-west dike swarm, that is, an orientation parallel to, and incompatible with, the present minimum orientation S_h measured in PTA2. A hypothesis is that this dike system was emplaced in a state of stress that was not affected by the gravitational stress induced by the Mauna Loa edifice, that is, prior to buildup of Mauna Loa volcano.

Although the borehole breakout orientation is constant in the borehole, the shape and size of the enlargements change within PTA2. A correlation exists between the shape and size of the borehole breakouts with volcanic facies. Within the same lithology, a variation in breakout development has been observed and correlated to contrasts in both the amplitude image and volcanic intra-facies (Figure 11). Pāhoehoe and ‘a’ā lava flows contain a clear inner layering linked to intra-facies development of individual flow units (Self et al., 1998). In general terms, pāhoehoe lava flows commonly comprise an upper vesicular zone (UVZ) or upper crust, a dense poorly vesicular interior, and a lower vesicular zone (LVZ) or lower flow crust at the base (Katz & Cashman, 2003) although variations such as spongey pāhoehoe occur (Walker, 1989; Wilmoth & Walker, 1993). ‘a’ā lava flows show instead auto-brecciated upper and lower crusts separated by a dense poorly vesicular interior which may display strained and irregular vesicles alongside vesicle bands (Katz & Cashman, 2003). These different intra-facies can be clearly recognized in the acoustic amplitude images.

Low contrast in the amplitude image has been interpreted as layers with vesicles or breccia and can be calibrated by core observations. High amplitude values reflect a lower presence of vesicles/breccia (lower porosity) and also lower percentages of clays, a common feature linked to alteration at lava flow margins. Intrusions often show high amplitude values associated with well-developed breakouts (Figure 11c).

The intra-facies variations are confirmed by cross-checking the acoustic image intervals with the core, and the relative strength is inferred based on numerous literature studies which confirm that strength of volcanic rocks decreases both with increasing porosity (Al-Harthi et al., 1999; Heap et al., 2014) and alteration (Planke et al., 1999; Schiffman et al., 2006). These results give clear evidence for the anisotropic accumulation of stress within the PTA2 borehole. Stronger, more coherent and less compressible facies and intra-facies are capable of storing higher stresses in a precritical stress state than the weaker facies and intra-facies. This observation is consistent with the observations of Schiffman et al. (2006) from the HSDP borehole where predicted UCS for different facies was linked to slope stability of the island of Hawai'i. Our observations further demonstrate that the highly anisotropic nature of strength within layered lava flow dominated sequences may promote differential slip when exposed to applied topographic loads or variable remote stresses. Therefore, the tendency for slip along flow boundaries and associated edifice stability may be significantly influenced by the stacking pattern of evolving lava fields, the geometry of subsurface intrusions, and the orientation of both relative to evolving applied stresses such as topographic loading through time. This study therefore provides the basis for a quantitative investigation into the stress magnitudes and anisotropy of the island of Hawai'i utilizing petrophysical testing of the PTA2 core.

7. Conclusions

The contemporary stress field of the southwestern flank on Mauna Kea volcano has been determined from borehole breakout analysis of the PTA2 borehole drilled in the saddle region of the island of Hawai'i. The location of the PTA2 borehole enables unique insights into the stress field in an area where only limited other stress indicators, such as faulting and focal mechanisms, are available. Our study reveals how the shallow subsurface stress state within composite volcanic islands evolves during edifice growth with implications for the improved understanding of slope stability, magma ascent, and earthquake monitoring on the island of Hawai'i and in similar settings.

Based on this analysis of the PTA2 breakout data, we conclude the following:

1. This study provides the first documentation of the subsurface in situ stress state between the major island forming shield volcanoes of Mauna Loa and Mauna Kea.
2. The borehole breakout analysis shows a clear and consistent orientation along the PTA2 borehole with a mean orientation of N106° with very low standard deviation for a total length of 310 m within seven main zones of breakouts. This corresponds to a maximum horizontal stress (S_H) orientation of N16°.
3. The orientation of the present-day stress field at Mauna Kea volcano deviates significantly from that of the plate forces and regional tectonic stress field which give a dominant NW-SE orientation of S_H. The orientation of the local stress field within the saddle region is dominantly controlled by the competing gravitational effects of the two large topographic masses of Mauna Loa and Mauna Kea volcanoes.
4. Our study suggests that the incremental growth of the younger Mauna Loa imparted an equivalently incremental stress addition to the southern flank of Mauna Kea. Given the important role of in situ stresses on magma propagation, this temporal change likely influenced the transport of magma in the area between the shield volcanos through time.
5. The variability of breakout shape and extent is associated with the different strengths of volcanic facies and intra-facies. Strong lava flow interiors and intrusions are capable of focusing greater stress accumulations than weaker lava flow margins. These findings have important implications for how applied stress is stored and dissipated in volcanic edifices and may have important implications for slope stability through time.

Data Availability Statement

Seismic data are available from National Earthquake Information Center (NEIC) https://earthquake.usgs.gov/contactus/golden/neic.php. The acoustic borehole images and all other downhole logs are published in the GFZ Data Service http://doi.org/10.5880/GFZ.4.8.2019.011.

Acknowledgments

This PTA2 borehole investigation was funded by the International Continental Scientific Drilling Program (ICDP) and by VMAPP (Volcanic Margin Petroleum Prospectivity) project (VBPR/DougalEARTH/TGS) in collaboration with the Humu'ula Groundwater Research Project. D. A. J. and S. P. are partly funded through a Norwegian Research Council Centres of Excellence project (project number 223272, CEED). We thank Marco Groh for the logging operations. We thank two anonymous reviewers for the comments and suggestions. We are particularly grateful to the Associate Editor Mike Poland for his valuable comments and his critical review that greatly improved the manuscript.

References

Acocella, V., & Neri, M. (2009). Dike propagation in volcanic edifices: Overview and possible developments. *Tectonophysics*, *471*(1–2), 67–77. https://doi.org/10.1016/j.tecto.2008.10.002

Al-Harthi, A. A., Al-Amri, R. M., & Shehata, W. M. (1999). The porosity and engineering properties of vesicular basalt in Saudi Arabia. *Engineering Geology*, *54*(3–4), 313–320. https://doi.org/10.1016/S0013-7952(99)00050-2

Amadei, B., & Stephansson, O. (1997). *Rock stress and its measurements* (p. 489). London: Chapman & Hall.

Appleman, D. E. (1987). James D. Dana and the origins of Hawaiian volcanology. In R. W. Decker, T. L. Wright, & P. H. Stauffer (Eds.), *The U.S. exploring expedition in Hawaii, 1840–41, of volcanism in Hawaii* (Chap. 60, Vol. 2, pp. 1607–1618). Washington, USA: U.S. Geological Survey Professional Paper. Retrieved from http://pubs.usgs.gov/pp/1987/1350/

Artyushkov, E. V. (1973). Stresses in the lithosphere caused by crustal thickness inhomogeneities. *Journal of Geophysical Research*, *7832*, 7675–7708. https://doi.org/10.1029/JB078i032p07675

Babcock, E. A. (1978). Measurement of subsurface fractures from dipmeter logs. AAPG Bulletin, 627, 1111–1126. Reprinted in 1990. In N. H. Foster, & E. A. Beaumont (Eds.), *Formation evaluation II—Log interpretation* (Reprint Series No. 17, pp. 457–472). Tulsa, USA: American Association of Petroleum Geologists Treatise of Petroleum Geology.

Barnard, W. M. (1995). *Mauna Loa volcano: Historical eruptions, exploration, and observations (1779-1910)* (Vol. 92, pp. 1–19). Washington DC: American Geophysical Union Geophysical Monograph Series.

Barton, C., & Moos, D. (2010). Geomechanical wellbore imaging: Key to managing the asset life style. In M. Pöppelreiter, C. García-Carballido, & M. Kraaijveld (Eds.), *Dipmeter and borehole image log technology* (Vol. 92, pp. 81–112). Tulsa, USA: American Association of Petroleum Geologists Memoir.

Bell, J. S. (1996a). In situ stresses in sedimentary rocks (Part 1): Measurement techniques. *Geoscience Canada*, *23*(2), 85–100. https://journals.lib.unb.ca/index.php/GC/article/view/3902

Bell, J. S. (1996b). In situ stresses in sedimentary rocks (Part 2): Applications of stress measurements. *Geoscience Canada*, *23*(3), 135–153. https://journals.lib.unb.ca/index.php/GC/article/view/3910

Bell, J. S., & Gough, D. I. (1979). Northeast-southwest compressive stress in Alberta: Evidence from oil wells. *Earth and Planetary Science Letters*, *45*(2), 475–482. https://doi.org/10.1016/0012-821X(79)90146-8

Borgia, A., & Treves, B. (1992). Volcanic plates overriding the ocean crust: Structure and dynamics of Hawaiian volcanoes. In L. M. Parson B. J. Murton & P. Browning, et al. (Eds.), *Ophiolites and their modern oceanic analogues* (Vol. 60, pp. 277–299). Bath, UK: Geological Society London; Special Publication.

Cannon, E. C., Bürgmann, R. A., Crone, J., Machette, M. N., & Dart, R. L. (2007). Map and data for Quaternary faults and fault systems on the island of Hawaii. In *U.S. Geological Survey Open-File Report* (pp. 1–81). Reston, Virginia, USA: U.S. Geological Survey Government Printing Office. https://pubs.usgs.gov/of/2007/1284/

Chadwick, W. W., & Dieterich, J. H. (1995). Mechanical modeling of circumferential and radial dike intrusion on Galapagos volcanoes. *Journal of Volcanology and Geothermal Research*, *66*(1-4), 37–52. https://doi.org/10.1016/0377-0273(94)00060-T

Clague, D. A., & Dalrymple, G. B. (1987). The Hawaiian-Emperor volcanic chain, Part I. In R. W. Decker, T. L. Wright, & P. H. Stauffer (Eds.), *Volcanism in Hawaii* (Chap. 1, Vol. 1, pp. 5–54). Washington, USA: U.S. Geological Survey Government Printing Office. https://pubs.usgs.gov/pp/1987/1350/pdf/chapters/pp1350_ch1.pdf

Delcamp, A., van Wyk de Vries, B., & James, M. R. (2008). The influence of edifice slope and substrata on volcano spreading. *Journal of Volcanology and Geothermal Research*, *177*(4), 925–943. https://doi.org/10.1016/j.jvolgeores.2008.07.014

Dieterich, J. H. (1988). Growth and persistence of Hawaiian Volcanic Rift Zones. *Journal of Geophysical Research*, *93*(B5), 4258–4270. https://doi.org/10.1029/JB093iB05p04258

Eakins, B., Robinson, J. E., Kanamatsu, T., Naka, J., Smith, J. R., Takahashi, E., & Clague, D. A. (2003). *Hawaii's volcanoes revealed: U.S. Geological Survey Geological Investigations Series Map I-2809, 1 sheet*. Denver, Colorado, USA: U.S. Geological Survey. http://geopubs.wr.usgs.gov/i-map/i2809/

Engelder, T. (1993). *Stress regimes in the lithosphere*. Princeton: Princeton University Press.

Fiske, R. S., & Jackson, E. D. (1972). Orientation and growth of Hawaiian volcanic rifts: The effect of regional structure and gravitational stresses. *Proceedings of the Royal Society of London. Series A: Mathematical and Physical Sciences*, *329*, 299–326. https://doi.org/10.1098/rspa.1972.0115

Flanigan, V. J., & Long, C. L. (1987). Aeromagnetic and near-surface electrical expression of the Kilauea and Mauna Loa volcanic rift systems. In R. W. Decker, T. L. Wright, & P. H. Stauffer (Eds.), *Volcanism in Hawaii* (Vol. 1, pp. 935–946). Washington, USA: U.S. Geological Survey Professional Paper 1350.

Flinders, A., Ito, G., Garcia, M. O., Sinton, J. M., Kauahikaua, J., & Taylor, B. (2013). Intrusive dike complexes, cumulate cores, and the extrusive growth of Hawaiian volcanoes. *Geophysical Research Letters*, *40*, 3367–3373. https://doi.org/10.1002/grl.50633

Fornari, D. J. (1987). The geomorphic and structural development of Hawaiian submarine rift zones. In R. W. Decker, T. L. Wright, & P. H. Stauffer (Eds.), *Volcanism in Hawaii* (Vol. 1, pp. 125–132). Washington, USA: U.S. Geological Survey Professional Paper 1350.

Frey, F. A., Garcia, M. O., Wise, W. S., Kennedy, A., Gurriet, P., & Albarede, F. (1991). The evolution of Mauna Kea volcano, Hawaii: Petrogenesis of tholeiitic and alkalic basalts. *Journal of Geophysical Research*, *96*(B9), 14,347–14,375. https://doi.org/10.1029/91JB00940

Frey, F. A., Wise, W. S., Garcia, M. O., West, H., Kwon, S. T., & Kennedy, A. (1990). Evolution of Mauna Kea volcano, Hawaii: Petrologic and geochemical constraints on postshield volcanism. *Journal of Geophysical Research*, *95*(B2), 1271–1300. https://doi.org/10.1029/JB095iB02p01271

Galland, O., Holohan, E. P., van Wyk de Vries, B., & Burchardt, S. (2018). Laboratory modelling of volcano plumbing systems: A review. In C. Breitkreuz, & S. Rocchi (Eds.), *Physical geology of shallow magmatic systems—Dykes, sills and laccoliths* (pp. 147–214). Berlin Heidelberg: Springer.

Garcia, M. O., Haskins, E. H., Stolper, E. M., & Baker, M. B. (2007). Stratigraphy of the Hawai'i Scientific Drilling Project core (HSDP2): Anatomy of a Hawaiian shield volcano. *Geochemistry, Geophysics, Geosystems*, *8*, Q02G20. https://doi.org/10.1029/2006GC001379

García-Carballido, C., Boon, J., & Tso, N. (2010). Data management and quality control of dipmeter and borehole image log data. In M. Pöppelreiter, C. García-Carballido, & M. Kraaijveld (Eds.), *Dipmeter and borehole image log technology* (Vol. 92, pp. 39–49). Tulsa, USA: AAPG Memoir.

Haimson, B. C., & Herrick, C. G. (1985). Borehole breakouts-anew tool for estimating in situ stress. In O. Stephansson (Ed.), *Rock stress and rock stress measurements* (pp. 271–280). Lulea: Centek Publishers.

Heap, M. J., Xu, T., & Chen, C. F. (2014). The influence of porosity and vesicle size on the brittle strength of volcanic rocks and magma. *Bulletin of Volcanology*, *76*(9), 856. https://doi.org/10.1007/s00445-014-0856-0

Heidbach, O., Rajabi, M., Cui, X., Fuchs, K., Müller, B., Reinecker, J., et al. (2018). The World Stress Map database release 2016: Crustal stress pattern across scales. *Tectonophysics*, *744*, 484–498. https://doi.org/10.1016/j.tecto.2018.07.007

Heidbach, O., Rajabi, M., Reiter, K., & Ziegler, M. (2016). *World stress map 2016*. Potsdam, Germany: GFZ Data Services. https://doi.org/10.5880/WSM.2016.002

Heidbach, O., Reinecker, J., Tingay, M., Müller, B., Sperner, B., Fuchs, K., & Wenzel, F. (2007). Plate boundary forces are not enough: Second- and third-order stress patterns highlighted in the World Stress Map database. *Tectonics*, *26*, TC6014. https://doi.org/10.1029/2007TC002133

Hergert, T., Heidbach, O., Reiter, K., Giger, S. B., & Marschall, P. (2015). Stress field sensitivity analysis in a sedimentary sequence of the Alpine foreland, northern Switzerland. *Solid Earth*, *6*(2), 533–552. https://doi.org/10.5194/se-6-533-2015

Hillis, R. R., & Reynolds, S. D. (2000). The Australian Stress Map. *Journal of the Geological Society, London*, *157*(5), 915–921. https://doi.org/10.1144/jgs.157.5.915

Holcomb, R. T., Nelson, B. K., Reiners, P. W., & Awyer, N. L. (2000). Overlapping volcanoes—The origin of Hilo Ridge, Hawaii. *Geology*, *286*, 547–550. https://doi.org/10.1130/0091-7613(2000)028%3C0547:ovtooh%3E2.3.co;2

Hyndman, D. W., & Alt, D. (1987). Radial dikes, laccoliths, and gelatin models. *Journal of Geology*, *95*(6), 763–774. https://doi.org/10.1086/629176

Jerram, D. A., Millett, J. M., Kück, J., Thomas, D., Planke, S., Haskins, E., et al. (2019). Understanding volcanic facies in the subsurface: A combined core, wireline logging and image log data-set from the PTA2 and KMA1 boreholes, Big Island, Hawai'i. *Scientific Drilling*, *7*, 1–18. https://doi.org/10.5194/sd-7-1-2019

Katz, M. G., & Cashman, K. V. (2003). Hawaiian lava flows in the third dimension: Identification and interpretation of pahoehoe and 'a'a distribution in the KP-1 and SOH-4 cores. *Geochemistry, Geophysics, Geosystems*, *4*(2), 8705. https://doi.org/10.1029/2001GC000209

Kervyn, M., Ernst, G. G. J., van Wyk de Vries, B., Mathieu, L., & Jacobs, P. (2009). Volcano load control on dyke propagation and vent distribution: Insights from analogue modeling. *Journal of Geophysical Research*, *114*, B03401. https://doi.org/10.1029/2008JB005653

Kirsch, G. (1898). Die Theorie der Elastizität und die Beaurforisse der Festigkeitslehre. In *Z. Ver Deut Ingen 1857 1968* (Vol. 42, pp. 797–807). Berlin, Germany.

Klein, F. W. (2016). Lithospheric flexure under the Hawaiian volcanic load: Internal stresses and a broken plate revealed by earthquakes. *Journal of Geophysical Research: Solid Earth*, *121*, 2400–2428. https://doi.org/10.1002/2015JB012746

Klein, F. W., & Koyanagi, R. Y. (1989). The seismicity and tectonics of Hawaii. In J. Winterer, D. Hussong, & R. Decker (Eds.), *The Eastern Pacific Ocean and Hawaii, Volume N of the Decade of North American Geology* (pp. 238–252). Boulder, CO: Geological Society of America.

Le Corvec, N., & McGovern, P. J. (2018). The effect of ocean loading on the growth of basaltic ocean island volcanoes and their magmatic plumbing system. *Frontiers in Earth Science*, *6*(119). https://doi.org/10.3389/feart.2018.00119

Le Corvec, N., & Walter, T. R. (2009). Volcano spreading and fault interaction influenced by rift zone intrusions: Insights from analogue experiments analyzed with digital image correlation technique. *Journal of Volcanology and Geothermal Research*, *183*(3-4), 170–182. https://doi.org/10.1016/j.jvolgeores.2009.02.006

Lin, G., & Okubo, P. G. (2016). A large refined catalog of earthquake relocations and focal mechanisms for the island of Hawai'i and its seismotectonic implications. *Journal of Geophysical Research: Solid Earth*, *121*, 5031–5048. https://doi.org/10.1002/2016JB013042

Liu, L., & Zoback, M. D. (1992). The effect of topography on the state of stress in the crust' application to the site of the Cajon Pass Scientific Drilling Project. *Journal of Geophysical Research*, *97*(B4), 5095–5108. https://doi.org/10.1029/91JB01355

Lofts, J. C., & Bourke, L. T. (1999). The recognition of artefacts from acoustic and resistivity borehole imaging devices. *Geological Society, London, Special Publications*, *159*(1), 59–76. https://doi.org/10.1144/GSL.SP.1999.159.01.03

McGovern, P. J. (2007). Flexural stresses beneath Hawaii: Implications for the October 15, 2006, earthquakes and magma ascent. *Geophysical Research Letters*, *34*, L23305. https://doi.org/10.1029/2007GL031305

McGuire, W. J., & Pullen, A. D. (1989). Location and orientation of eruptive fissures and feeder-dykes at Mount Etna; influence of gravitational and regional tectonic stress regimes. *Journal of Volcanology and Geothermal Research*, *38*(3-4), 325–344. https://doi.org/10.1016/0377-0273(89)90046-2

Millett, J. M., Blischke, A., Planke, S., Jerram, D. A., Árnadóttir, S., Pierdominici, S., et al. (2018). Borehole imaging log analysis, a volcanic facies and structural analysis tool: Case examples from Hawai'i and Iceland. Paper presented at EGU General Assembly 2018. *Geophysical Research Abstracts*, *20*, EGU2018–15895.

Moore, J. G. (1970). Relationship between subsidence and volcanic load, Hawaii. *Bulletin of Volcanology*, *34*(2), 562–576. https://doi.org/10.1007/BF02596771

Moore, J. G., & Chadwick, W. W. Jr. (1995). Offshore geology of Mauna Loa and adjacent areas, Hawaii. In J. M. Rhodes & J. P. Lockwood (Eds.), *Mauna Loa revealed—Structure, composition, history, and hazards* (Vol. 92, pp. 21–44). Washington, USA: American Geophysical Union Geophysical Monograph.

Moore, J. G., & Clague, D. A. (1992). Volcano growth and evolution of the island of Hawaii. *Geological Society of America Bulletin*, 10411, 1471–1484. https://doi.org/10.1130/0016-7606(1992)104%3C1471:vgaeot%3E2.3.co;2

Moore, J. G., Normark, W. R., & Holcomb, R. T. (1994). Giant Hawaiian landslides. *Annual Review of Earth and Planetary Sciences*, *22*(1), 119–144. https://doi.org/10.1146/annurev.ea.22.050194.001003

Morgan, J. K., Park, J., & Zelt, C. A. (2010). Rift zone abandonment and reconfiguration in Hawaii: Mauna Loa's Ninole rift zone. *Geology*, *38*(5), 471–474. https://doi.org/10.1130/G30626.1

Morin, R. H., & Wilkens, R. H. (2005). Structure and stress state of Hawaiian island basalts penetrated by the Hawaii Scientific Drilling Project deep core hole. *Journal of Geophysical Research*, *110*, B07404. https://doi.org/10.1029/2004JB003410

Muller, J. R., Ito, G., & Martel, S. J. (2001). Effects of volcano loading on propagation in an elastic half-space. *Journal of Geophysical Research*, *106*(B6), 11,101–11,113. https://doi.org/10.1029/2000JB900461

National Earthquake Information Center (NEIC) https://earthquake.usgs.gov/contactus/golden/neic.php

Pan, E., Amadei, B., & Savage, W. Z. (1995). Gravitational and tectonic stresses in anisotropic rock with irregular topography. *International Journal of Rock Mechanics and Mining Sciences & Geomechanics*, *32*(3), 201–214. https://doi.org/10.1016/0148-9062(94)00046-6

Park, J., Morgan, J. K., Zelt, C. A., & Okubo, P. G. (2009). Volcano-tectonic implications of 3-D velocity structures derived from joint active and passive source tomography of the island of Hawaii. *Journal of Geophysical Research*, *114*, B09301. https://doi.org/10.1029/2008JB005929

Peterson, D. W., & Moore, R. B. (1987). Geologic history and evolution of geologic concepts, island of Hawaii. In R. W. Decker, T. L. Wright, & P. H. Stauffer (Eds.), *Volcanism in Hawaii* (Vol. 1, pp. 149–189). Washington, USA: U.S. Geological Survey Professional Paper 1350.

Pierdominici, S., & Heidbach, O. (2012). Stress field of Italy—Mean stress orientation at different depths and wave-length of the stress pattern. *Tectonophysics*, *532-535*, 301–311. https://doi.org/10.1016/j.tecto.2012.02.018

Planke, S., Cerney, B., Bücker, C. J., & Nilsen, O. (1999). Alteration effects on petrophysical properties of subaerial flood basalts: Site 990, Southeast Greenland margin. In *Proceedings of the Ocean Drilling Program, Scientific Results* (Vol. 163, pp. 17–28). College Station, Texas, USA: Ocean drilling program, College Station.

Plumb, R. A., & Hickman, S. H. (1985). Stress-induced borehole elongation: A comparison between the four-arm dipmeter and the borehole televiewer in the Auburn Geothermal Well. *Journal of Geophysical Research*, *90*(B7), 5513–5521. https://doi.org/10.1029/JB090iB07p05513

Poland, M. P., Garcia, M. O., Camp, V. E., & Grunder, A. (2018). *Field volcanology: A tribute to the distinguished career of Don Swanson* (Vol. 538). Boulder, CO, USA: Geological Society of America. https://doi.org/10.1130/SPE538

Porter, S. C. (1987). Pleistocene subglacial eruptions on Mauna Kea. In R. W. Decker, T. L. Wright, & P. H. Stauffer (Eds.), *Volcanism in Hawaii* (pp. 587–598). Washington, USA: USGS prof. Paper 1350

Pritchard, M. E., Rubin, A. M., & Wolfe, C. J. (2007). Do flexural stresses explain the mantle fault zone beneath Kilauea volcano? *Geophysical Journal International*, *168*(1), 419–430. https://doi.org/10.1111/j.1365-246X.2006.03169.x

Reinecker, J., Tingay, M., & Müller, B. (2016). Borehole breakout analysis from four-arm caliper logs. World Stress Map Project. Guidelines: Four-arm caliper logs. In O. Heidbach, A. Barth, B. Müller, J. Reinecker, O. Stephansson, M. Tingay, & A. Zang (Eds.), *WSM quality ranking scheme, database description and analysis guidelines for stress indicator* (Chapter 4, pp. 27–32). *World Stress Map Technical Report16–01*. Potsdam, Germany: GFZ German Research Centre for Geosciences. http://www.world-stress-map.org/fileadmin/wsm/pdfs/WSM_TR_16-01.pdf

Sahara, D. P., Schoenball, M., Kohl, T. T., & Müller, B. I. R. (2014). Impact of fracture networks on borehole breakout heterogeneities in crystalline rock. *International Journal of Rock Mechanics and Mining Sciences*, *71*, 301–309. https://doi.org/10.1016/j.ijrmms.2014.07.001

Schiffman, P., Watters, R. J., Thompson, N., & Walton, A. W. (2006). Hyaloclastites and the slope stability of Hawaiian volcanoes: Insights from the Hawaiian Scientific Drilling Project's 3-km drill core. *Journal of Volcanology and Geothermal Research*, *151*(1-3), 217–228. https://doi.org/10.1016/j.jvolgeores.2005.07.030

Self, S., Keszthelyi, L., & Thordarson, T. (1998). The importance of pāhoehoe. *Annual Review of Earth and Planetary Sciences*, *261*, 81–110. https://doi.org/10.1146/annurev.earth.26.1.81

Sharp, W. D., & Clague, D. A. (2006). 50-Ma initiation of Hawaiian-Emperor bend records major change in Pacific Plate motion. *Science*, *313*(5791), 1281–1284. https://doi.org/10.1126/science.1128489

Sherrod, D. R., Sinton, J. M., Watkins, S. E., & Brunt, K. M. (2007). Geological map of the state of Hawaii. In *Open File report 2007–1089* (pp. 44–48). United States Geological Survey. http://pubs.usgs.gov/of/2007/1089

Thomas, D. (2016). *Magnetotelluric and audio magnetotelluric surveys on Department of Hawaiian home lands Mauna Kea east flank. Final Report*. Hilo, Hawaii, USA: Hawaii Institute of Geophysics and Planetology Center for the Study of Active Volcanoes. https://energy.hawaii.gov/wp-content/uploads/2011/10/DHHLGeophysicalSurveysRpt_3.29.17.pdf

Tilling, R. I., Kauahikaua, J. P., Brantley, S. R., & Neal, C. A. (2014). The Hawaiian volcano observatory—A natural laboratory for studying basaltic volcanism. In M. P. Poland, T. J. Takahashi, & C. M. Landowski (Eds.), *Characteristics of Hawaiian volcanoes* (Chap. 2, pp. 1–64). Reston, Virginia, USA: U.S. Geological Survey Professional Paper 1801.

Tingay, M. R. P., Müller, B., Reinecker, J., & Heidbach, O. (2006). State and origin of the present-day stress field in sedimentary basins: New results from the world stress map project. In *Paper presented at Golden Rocks 2006, Conference paper, ARMA-06-1049, 41st U. S. Symposium on Rock Mechanics (USRMS): 50 Years of Rock Mechanics-Landmarks and Future Challenges*. Golden, Colorado: American Rock Mechanics Association.

Torsvik, T. H., Doubrovine, P. V., Steinberger, B., Gaina, C., Spakman, W., & Domeier, M. (2017). Pacific plate motion change caused the Hawaiian-Emperor Bend. *Nature Communications*, *8*(1), 15660. https://doi.org/10.1038/ncomms15660

Trice, R. (1999). Application of borehole image logs in constructing 3D static models of productive fracture networks in the Apulian Platform, Southern Apennines. In M. A. Lovell, G. Williamson, & P. K. Harvey (Eds.), *Borehole Imaging: applications and case histories* (Vol. 159, pp. 155–176). London, Special Publications: Geological Society.

Walcott, R. I. (1976). Lithospheric flexure, analysis of gravity anomalies, and the propagation of seamount chains. *Tectonophysics*, *19*, 431–438. https://doi.org/10.1029/gm019p0431

Walker, G. P. (1989). Spongy pahoehoe in Hawaii: A study of vesicle-distribution patterns in basalt and their significance. *Bulletin of Volcanology*, *51*(3), 199–209. https://doi.org/10.1007/BF01067956

Walter, T. R., & Amelung, F. (2006). Volcano-earthquake interaction at Mauna Loa volcano, Hawaii. *Journal of Geophysical Research*, *111*, B05204. https://doi.org/10.1029/2005JB003861

Watson, J. (1999). *The long trail of the Hawaiian hotspot*. United States Geological Survey.

West, H. B., Garcia, M. O., Frey, F. A., & Kennedy, A. (1988). Nature and cause of compositional variation among the alkalic cap lavas of Mauna Kea volcano, Hawaii. *Contributions to Mineralogy and Petrology*, *100*(3), 383–397. https://doi.org/10.1007/BF00379747

Wilmoth, R. A., & Walker, G. P. (1993). P-type and S-type pahoehoe: A study of vesicle distribution patterns in Hawaiian lava flows. *Journal of Volcanology and Geothermal Research*, *55*(1–2), 129–142. https://doi.org/10.1016/0377-0273(93)90094-8

Wilson, J. T. (1963). A possible origin of the Hawaiian Islands. *Canadian Journal of Physics*, *41*(6), 863–870. https://doi.org/10.1139/p63-094

Wolfe, C. J., Okubo, P. G., Ekström, G., Nettles, M., & Shearer, P. M. (2004). Characteristics of deep ≥13 km Hawaiian earthquakes and Hawaiian earthquakes west of 155.55°W. *Geochemistry, Geophysics, Geosystems*, *54*, Q04006. https://doi.org/10.1029/2003GC000618

Wolfe, E. W., & Morris, J. (1996). Geologic map of the island of Hawaii. In *U.S. Geological Survey miscellaneous investigations series map I-2524-A*. 18 p., 3 sheets, scale 1:100,000(–). Denver, CO, USA: U.S. Geological Survey. https://doi.org/10.3133/i2524A, https://pubs.usgs.gov/imap/2524a/report.pdf

Wolfe, E. W., Wise, W. S., & Dalrymple, G. B. (1997). The geology and petrology of Mauna Kea Volcano, Hawaii; a study of postshield volcanism. In *USGS Report* (Vol. 1557, p. 129). Denver, Colorado, USA: U.S. Geological Survey.

Zang, A., & Stephansson, O. (2010). *Stress field of the Earth's crust* (p. 322). Dordrecht, Heidelberg, London, New York: Ed. Springer Science and Business Media. https://doi.org/10.1007/978-1-4020-8444-7

Zemanek, J., Caldwell, R. L., Glenn, E. E., Jr Holcomb, S. V., Nortom, L. F., & Siraus, A. D. J. (1969). The borehole telewewer—A new logging concept for fracture location and other types of borehole inspection. *Journal of Petroleum Technology*, *264*, 762–774. https://doi.org/10.2118/2402-pa

Zoback, M. D. (2007). *Reservoir geomechanics* (449 p.). New York: Cambridge University Press.

Zoback, M. D., Moos, D. L., Mastin, L., & Anderson, R. N. (1985). Wellbore breakouts and in situ stress. *Journal of Geophysical Research*, *90*(B7), 5523–5530. https://doi.org/10.1029/JB090iB07p05523

Zoback, M.-L. (1992). First- and second-order patterns of stress in the lithosphere: The world stress map project. *Journal of Geophysical Research*, *97*(B8), 11,703–11,728. https://doi.org/10.1029/92JB00132

Zoback, M.-L., Zoback, M. D., Adams, J., Assumpção, M., Bell, S., Bergman, E. A., et al. (1989). Global patterns of tectonic stress. *Nature*, *341*(6240), 291–298. https://doi.org/10.1038/341291a0